

Chapter 4

OBSERVATIONAL RESULTS AND ANALYSES

4.1 Observational site

The coronal intensity measurements on the total solar eclipse of 11 August 1999 were conducted by Lake Hazar in Elazig, Turkey. The totality at this location ($38^{\circ}41'N, 039^{\circ}14'E$) lasted for 124 seconds. The second contact was at ~ 11.36 GMT. Also no clouds could be reported for the entire duration of the totality.

Figure (4.1) is a photograph of the total solar eclipse of 11 August 1999 taken from the Black Sea area. From figure (4.1) it is evident that the coronal brightness was almost uniformly distributed all around the sun. This was expected of the sun that was approaching maximum phase in 2000. This photograph also reveals a detached prominence in the southwest limb during the totality. Figure (4.2) depicts the path of the eclipse where the maximum duration of the totality occurred in Romania. Figure (4.3) shows the layout of MACS. The spectrograph lies on the metal box. The telescope, CCD-camera, and the computer were powered from a portable generator.



Figure (4.1). A photograph of the August 1999 eclipse from the Black Sea area. The photograph also reveals a detached prominence eruption above the southwest limb.

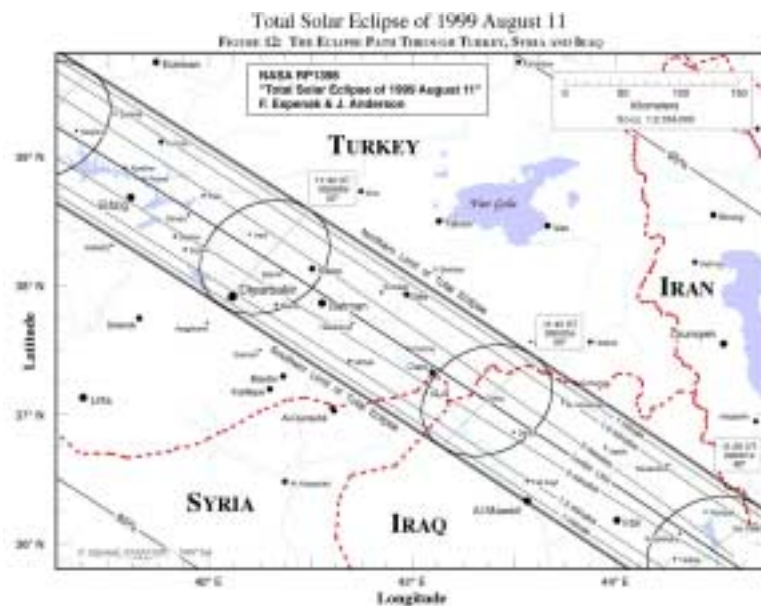


Figure (4.2). A map showing the path of the eclipse over Turkey.
Courtesy: NASA Reference Publication 1398



Figure (4.3). A picture showing the layout of MACS and the telescope. The telescope is on a polar mount and MACS is laid out on the metal box.

4.2 Spectra observed by MACS

Figure (4.4) shows the spectra due to the twenty-one fibers being exposed to the sky and the remaining four fibers being exposed to the mercury calibration lamp in Elazig, Turkey. The horizontal lines indicate the prominent absorption lines in the sky spectrum and the four bright dots on the two ends correspond to the emission line at 4046.7 angstrom in the mercury calibration lamp. This information was used to determine the wavelength scale and was determined to have a linear dispersion of 2.39 angstrom/pixel. The positions numbered from 1 to 4 are the locations corresponding to

the temperature and the wind sensitive wavelength positions, which is explained in chapter-2.

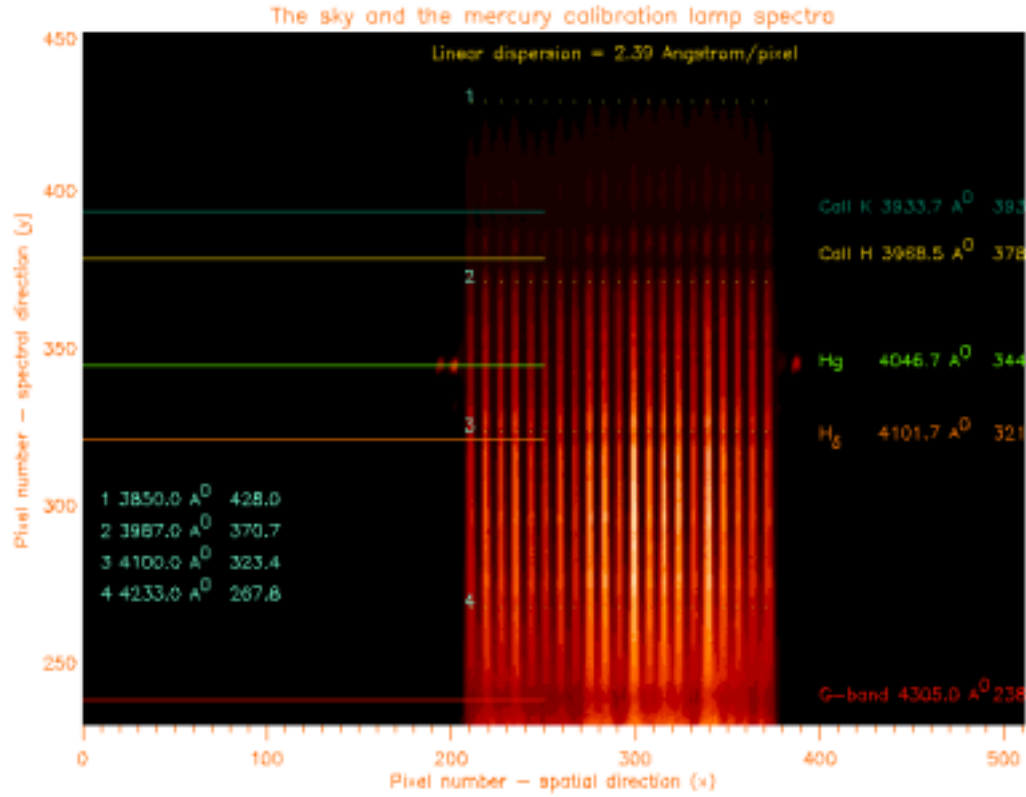
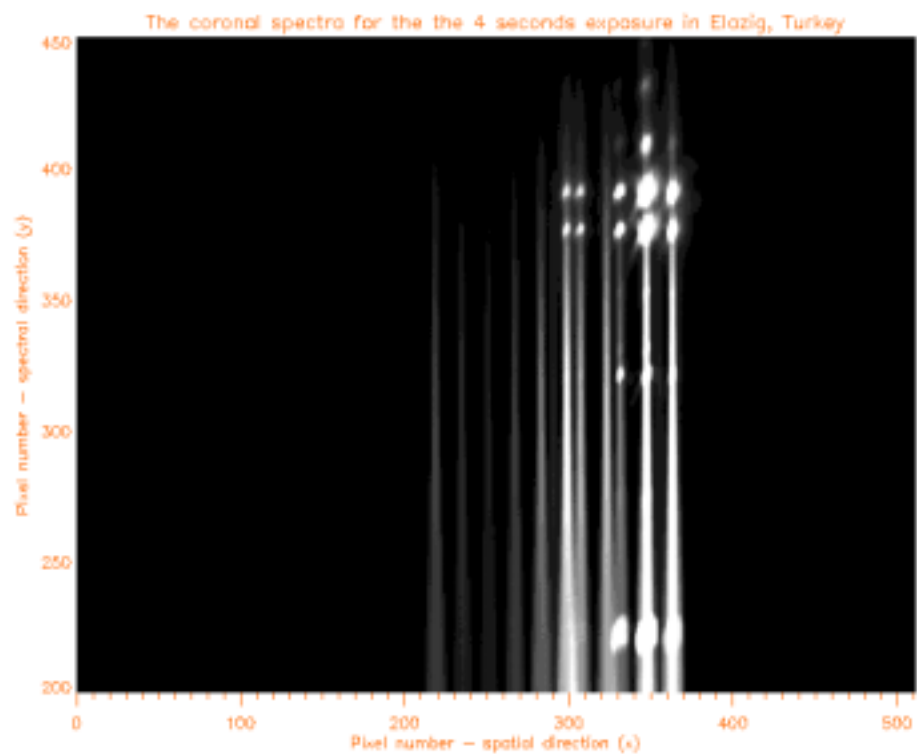


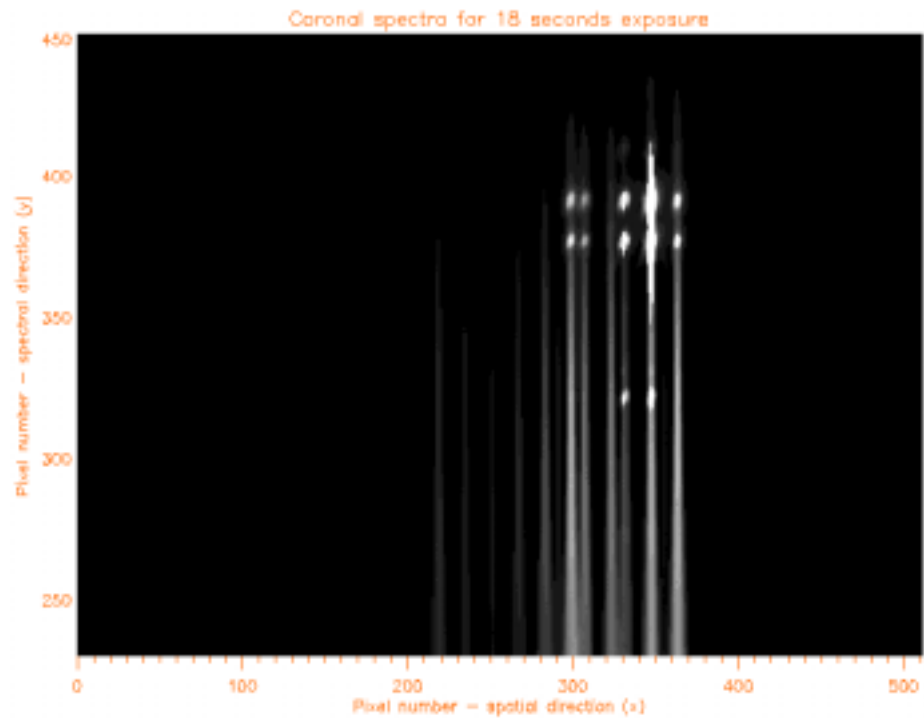
Figure (4.4). The spectra from twenty-one fibers exposed to the sky while four other fibers exposed to the mercury calibration lamp in Elazig, Turkey.

MACS was exposed to the coronal light during totality for duration of 4.0, 18.0 and 83.0-seconds. Figures (4.5 a), (4.5 b) and (4.5 c) show the spectra recorded by MACS for the above duration, respectively. Each vertical line corresponds to the spectrum from a single fiber with a total of twenty-one vertical lines corresponding to the twenty-one fibers located in the focal plane of the telescope.

(a)



(b)



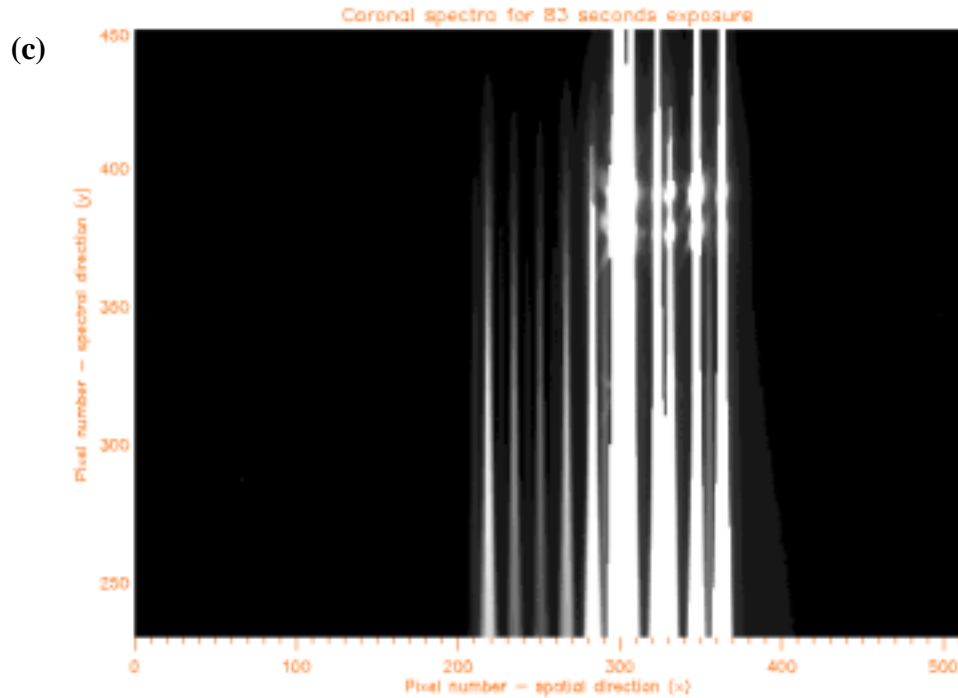


Figure (4.5 a, b, and c). The coronal spectra recorded by MACS for the exposure times 4.0, 8.0 and 83.0 seconds, respectively. Each vertical line corresponds to a spectrum from a single fiber. It is also clear that five of the fibers show emission lines.

4.3 Identifying the individual fiber location on the corona

Prior to the eclipse the sun was focused to the position identified by the moon during eclipse, as shown in figure (4.6). A solar filter attached at the front end of the telescope facilitated this process. The telescope was then allowed to track. Watching the direction of movement of the sun's image upon slewing the telescope due north and south with the auto controls the fiber #19 was oriented at the position perceived to be the earth's South Pole. Its relation to the heliographic coordinates was determined from the value listed for the P-angle for that day in, 'The Astronomical Almanac 1999'.

Figure (4.6) shows the envisaged location of the twenty-one fibers in the focal plane of the telescope during the eclipse. However the envisaged location could have drifted due to imperfect tracking or minute movements of the whole telescope structure for not being anchored on hard ground. Time constraints and the remoteness of the location compounded these problems. The term “envisaged” is emphasized because of the incapability of MACS at the present state to simultaneously record the image. This capability would have verified the exact location of the fiber rings during the eclipse.

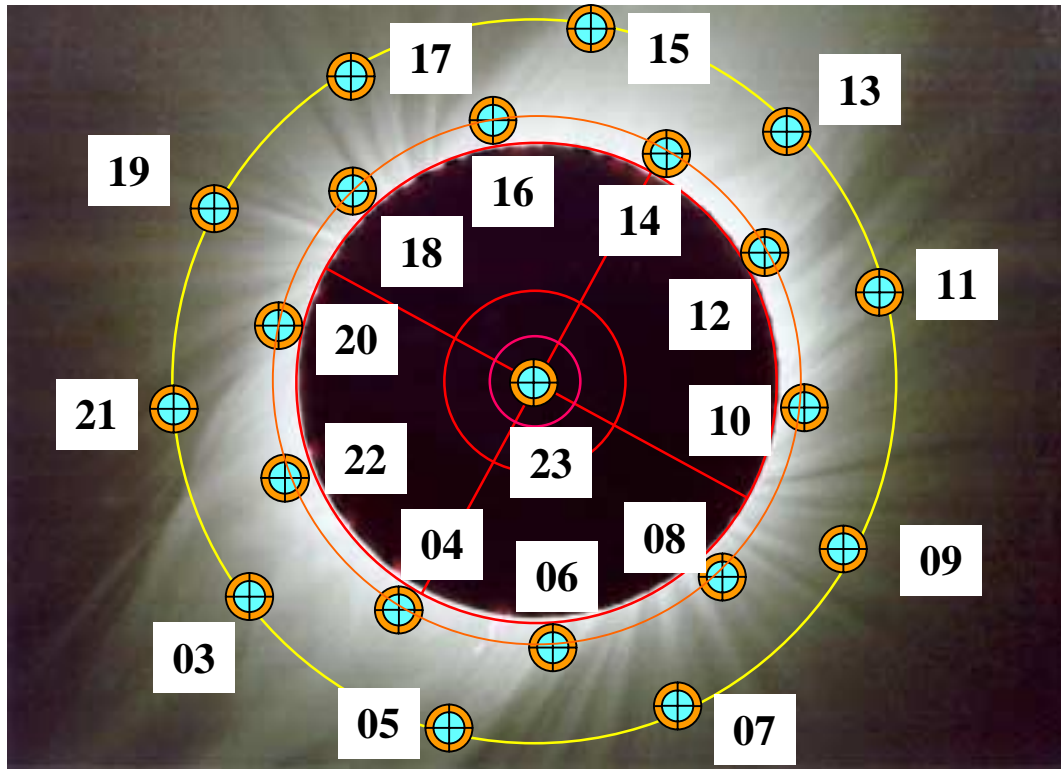


Figure (4.6). This picture shows the envisaged location of the twenty-one fibers in the focal plane during the eclipse. The inner and the outer rings correspond to 1.1 and 1.5 solar radii, respectively. The picture is not the actual eclipse on 11 August 1999. The fiber in the center was expected to record the background signal.

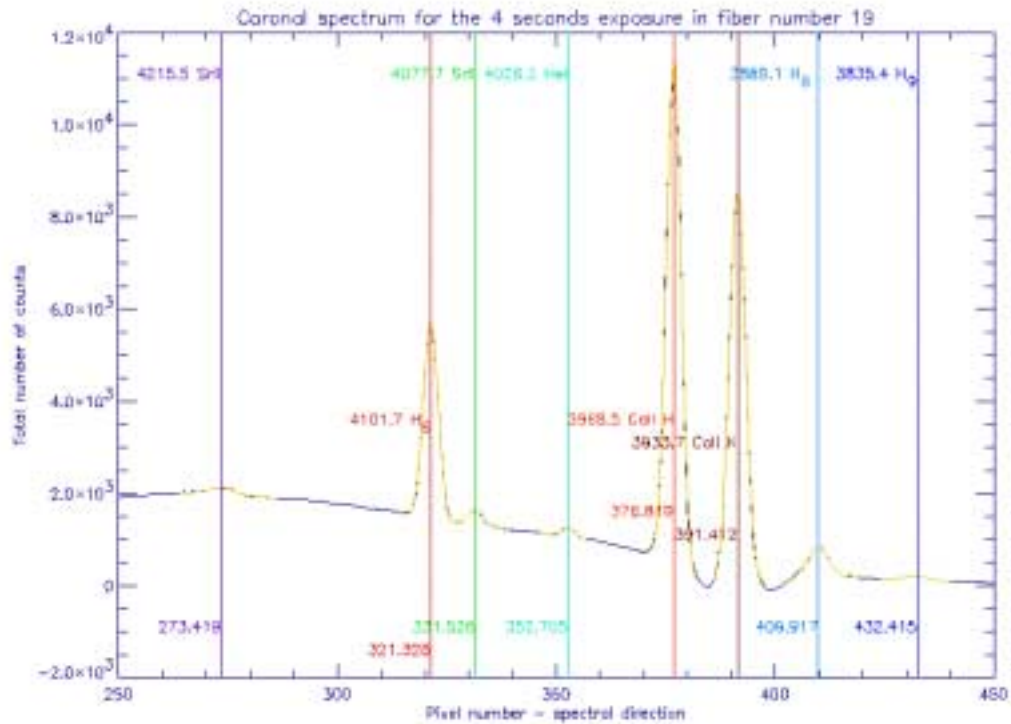
In order to identify the fiber orientation to a reasonable accuracy, some other information shown in the coronal spectra was utilized. This task was further aided by the very distinctive emission lines recorded in the spectra of five of the fibers as revealed in figure (4.5 a), figure (4.5 b), and figure (4.5 c). These emission lines are most pertinent to be from fibers exposed to prominence eruptions. Using imaging data at totality from other space and ground based solar instruments that are dedicated to observe specific solar features, it was now possible to infer the solar features that would have contributed to the emission lines in those fibers and accordingly orient the fibers.

The fibers that show emission lines, going from left to right in figure (4.5 a), figure (4.5 b), and figure (4.5 c), are the fibers numbered 22, 20, 19, 15 and 14 in figure (4.6). All the emission lines of fiber #19 correspond to the signatures of a prominence. Table (4.1) gives a list of prominence lines reported by Athay and Orrall (1957) from a prominence in the west limb of the total solar eclipse of 1952. Figure (4.7) shows the spectrum recorded by fiber #19. In this paper an emission line of Sr II listed at 3077.7 angstrom needs to be corrected as 4077.7 angstrom. Comparison between table (4.1) and figure (4.7) reveals that the fiber #19 had recorded all the prominence emission lines reported by Athay and Orrall (1957), that falls within the wavelength range of the detector in MACS.

Table (4.1) List of the emission lines reported by Athay and Orrall (1957) of a prominence from the total solar eclipse of 1952. In this paper the Sr II line at 4077.7 has been erroneously recorded as 3077.7 angstrom. In the following table only the emission lines that could lie within the wavelength range of MACS is enumerated.

Emission line	Wavelength (angstrom)
Sr II	4215.5
H ₆ (2-6)	4101.7
Sr II	4077.7
He I	4026.3
Ca II H	3968.5
Ca II K	3933.7
H ₈ (2-8)	3889.1
H ₉ (2-9)	3835.4

Figure (4.7) shows the spectrum recorded by the fiber #19 in the 4.0 seconds exposure. This is after averaging over three pixels about its center and subtracting the dark signal. However the spectrum is not yet corrected for the wavelength sensitivity of the telescope-spectrometer system.



From figure (4.7) and table (4.1) it is apparent that the fiber #19 had recorded all the prominence lines that fall within the wavelength range of the detector. The yellow curves superimposed on the spectrum are the gaussian curve fits. The wavelengths correspond to the peaks of the gaussian curves. However it needs to be yet ascertained whether the emission lines were correctly identified. This was verified by constructing a regression fit between the emission peaks and the peak positions. Figure (4.8) shows the result of the regression fit and the wavelength scale between different emission lines. These values give an average linear dispersion per pixel of 2.39 angstrom and matches with the linear dispersion per pixel calculated from the optical parameters of MACS.

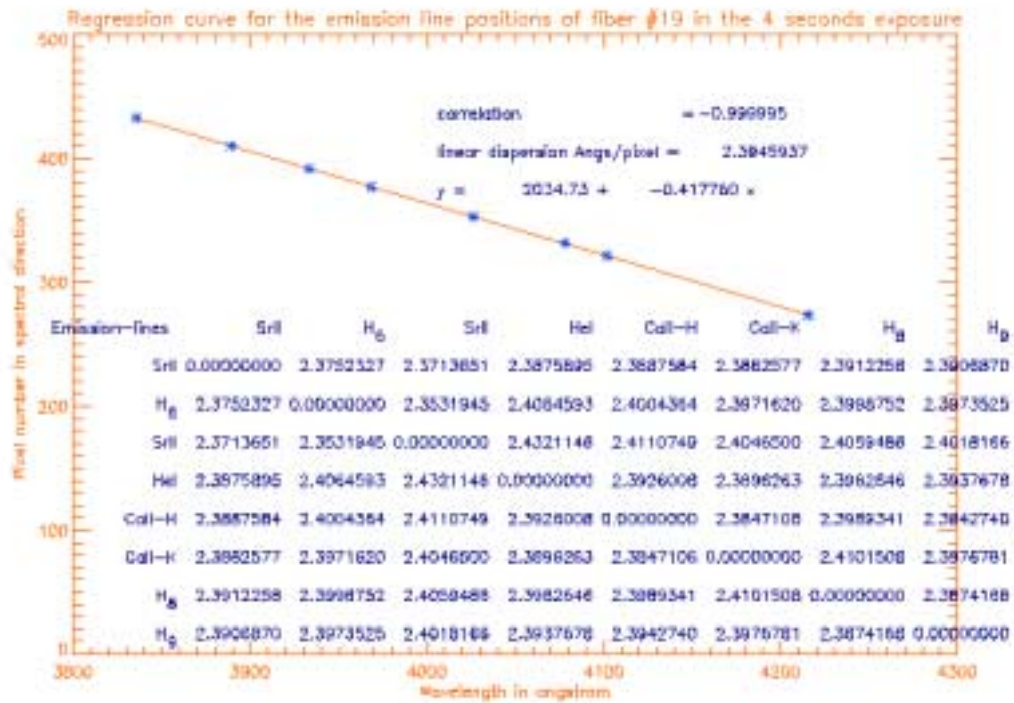


Figure (4.8). The regression fit between the emission line peaks and the peak positions of the fiber #19 in the 4.0 seconds exposure. The table incorporated shows the wavelength scale between any two-emission lines.

Furthermore, the spectrum recorded by the fiber #20 also shows all the emission lines from a prominence as listed in table (4.1). Figure (4.9) is the spectrum recorded by the fiber #20.

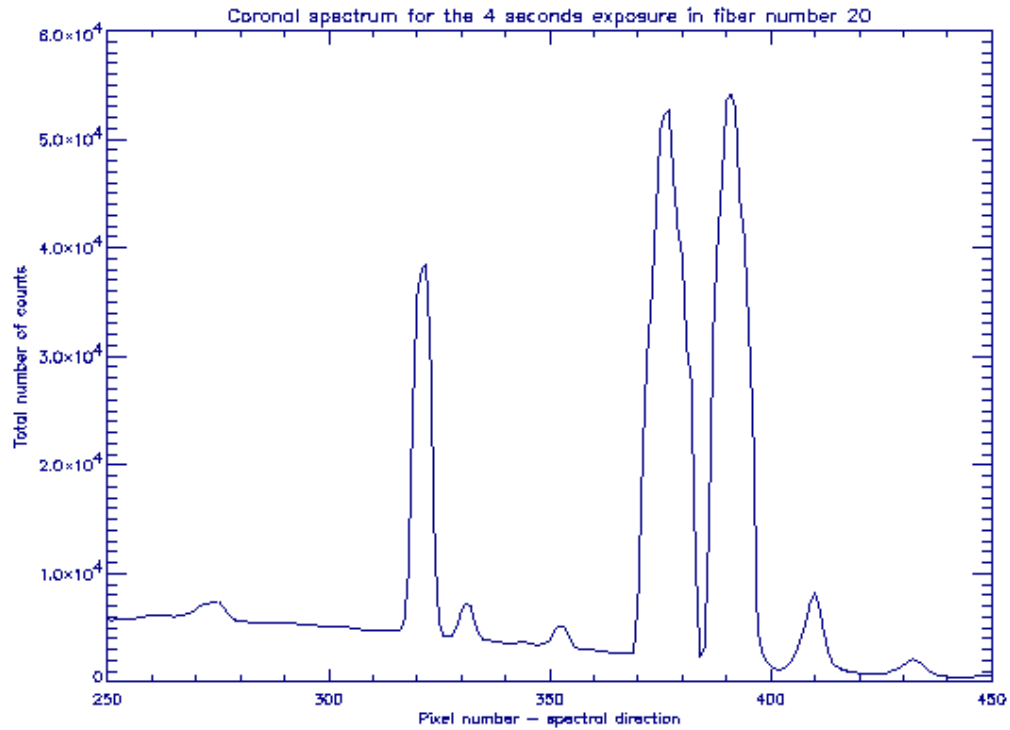


Figure (4.9). The spectrum recorded by the fiber #20 in the 4.0 seconds exposure. This too matches with all the emission lines recorded by the fiber #19 as shown in figure (4.7).

In table (4.2) is a list of emission lines, categorized as very strong and strong, from the flare of 18 September 1957 and reported by Jefferies, Smith and Smith (1959). Figure (4.10) shows the spectrum recorded by the fiber #22 in the 4.0 seconds exposure. This is after averaging over three pixels about its center and subtracting the dark signal. However the spectrum is not yet corrected for the wavelength sensitivity of the telescope-spectrometer system.

Table (4.2). List of the emission lines reported by Jefferies, Smith and Smith (1959) from the flare of 18 September 1957. This table only includes those emission lines categorized as very strong and strong. Also in this following table only the emission lines that could lie within the wavelength range of MACS is enumerated.

Emission line	Wavelength angstrom	Category
H₈	3889.1	strong
Ca II- K	3933.7	very strong
Ca II-H	3968.5	very strong
H_ε	3970.1	strong
H_δ	4101.7	very strong
H_γ	4340.5	very strong
HeI	4471.7	strong

Figure (4.10) showing the spectrum recorded by the fiber #20 does indicate that all but the **H_ε** line at 3970.1 angstrom listed in table (4.1) to be present. Since the linear dispersion is ~2.40 angstrom/pixel and, with the **H_ε** line at 3970.1 angstrom being only 2.0 angstrom away from the very strong Ca II-H line at 3968.5 angstrom, this may have caused this line to blend with the stronger line.

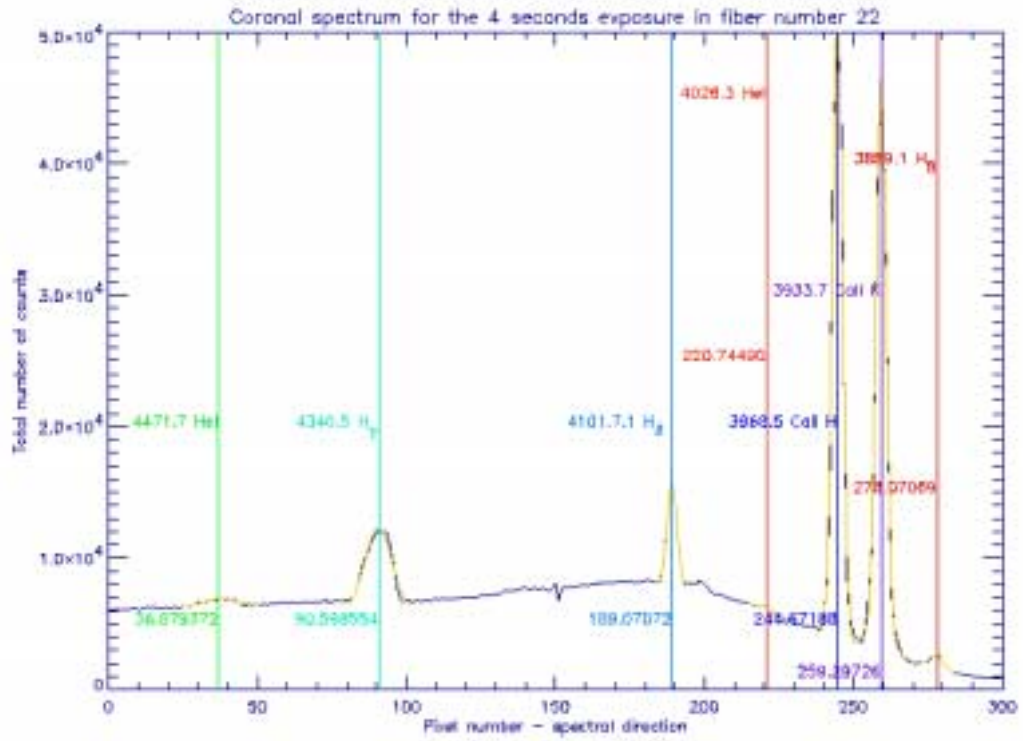


Figure (4.10). The spectrum recorded by the fiber #22 in the 4.0 seconds exposure. The emission lines and their corresponding wavelengths and pixel positions are identified.

Figure (4.11) shows the result of the regression fit and the wavelength scale between different emission lines of figure (4.10). These values give an average linear dispersion per pixel of 2.40 and matches with the linear dispersion per pixel calculated from the optical parameters for MACS, as listed in table (3.1).

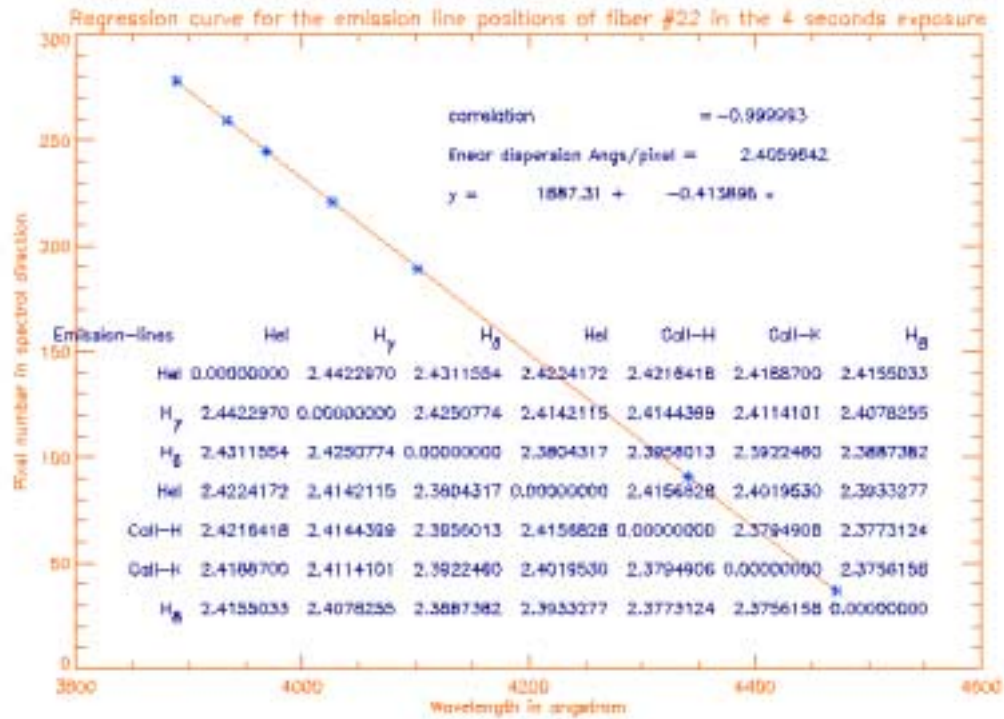


Figure (4.11). The regression fit between the emission line peaks and the peak positions of the fiber #19 in the 4.0 seconds exposure. The table incorporated shows the wavelength scale between any two-emission lines.

Based on the comparison on the spectra recorded by the fiber#19, fiber#20 and fiber #22 and the prominent emission lines expected of a prominence or a flare as listed in tables (4.1) and (4.2), respectively, it is reasonable to assume that these fibers were exposed to a prominence or a flare or to both of these features.

In order to identify the individual fiber location on the corona as accurately as possible the following analyses were performed.

1. Identifying the fibers exposed to prominence spectrum. The fibers #19, 20 and 22 were positively identified to have recorded the typical emission lines due to a prominence.
2. Orienting an eclipse photograph showing prominent eruptions with EIT images from SOHO on the day of the eclipse and matching these features. This matching was performed using the conspicuous prominence eruption identified at $\sim 68^{\circ}$ southwest in the EIT picture in 304 angstrom by SOHO at 11:26 UT with an eclipse photograph taken at $\sim 11:16$ UT from the Black Sea.
3. Drawing the polar axis of the earth, which is p-angle from the polar axis of the sun. The p-angle, which is the orientation of the polar axis of the sun with respect to the polar axis of the earth, was obtained from, 'The Astronomical Almanac 1999'.
4. Placing fiber #19 at the intersection point of the South Pole with the orbital circle at 1.5 solar radii. Prior to the eclipse the sun was focused to the position identified by the moon during eclipse, as shown in figure (4.6). A solar filter attached at the front end of the telescope facilitated this process. The telescope was then allowed to track. Watching the direction of movement of the sun's image upon slewing the telescope

due north and south with the auto controls the fiber #19 was oriented at the position perceived to be the earth's South Pole. The locations of the other fibers could be then determined based on their positions with respect to fiber #19.

Figure (4.12) shows the envisaged positions of the fibers on the corona based upon the above procedure.

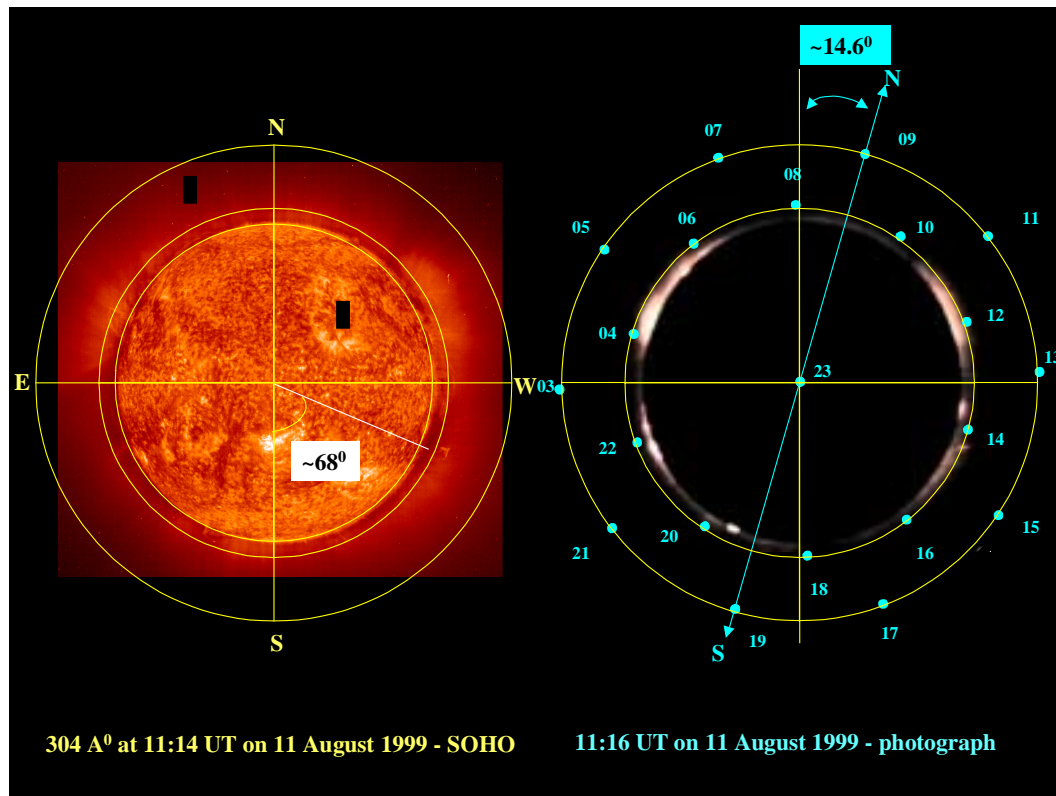


Figure (4.12). This is a comparison between solar image by SOHO in 304.0 angstrom at 11:14 UT and an eclipse photograph taken from the Black Sea at ~ 11:16UT. The orientation was made by matching the prominence eruption ~ 68° southwest in the SOHO image. The orientation of the polar axis of the sun with respect to the polar axis of the earth was obtained from the p-angle data given in, 'The Astronomical Almanac 1999' for 11 August 1999.

Figure (4.13), figure (4.14) and figure (4.15) are pictures of the sun taken by LASCO instrument on SOHO, EIT instrument on SOHO and radio image from Nancy and x-ray image by Yohkoh, respectively, on 11 August 1999.

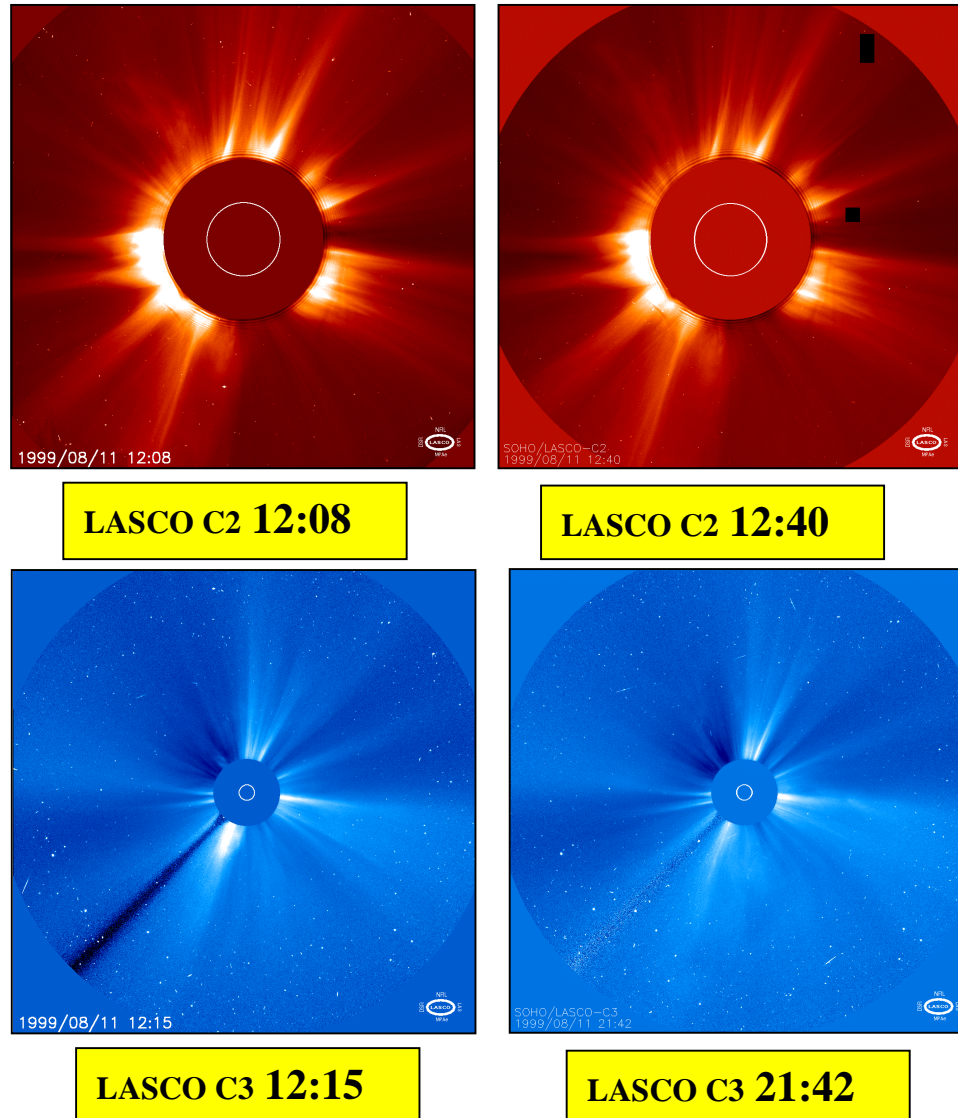


Figure (4.13). Images of the sun taken by the LASCO instrument on SOHO on the 11 August 1999. The numbers denote the time in UT. C2 and C3 are coronal images of the sun from 2.0 – 6.0 solar radii and 3.7 – 32.0 solar radii, respectively, using an externally occulted disk.

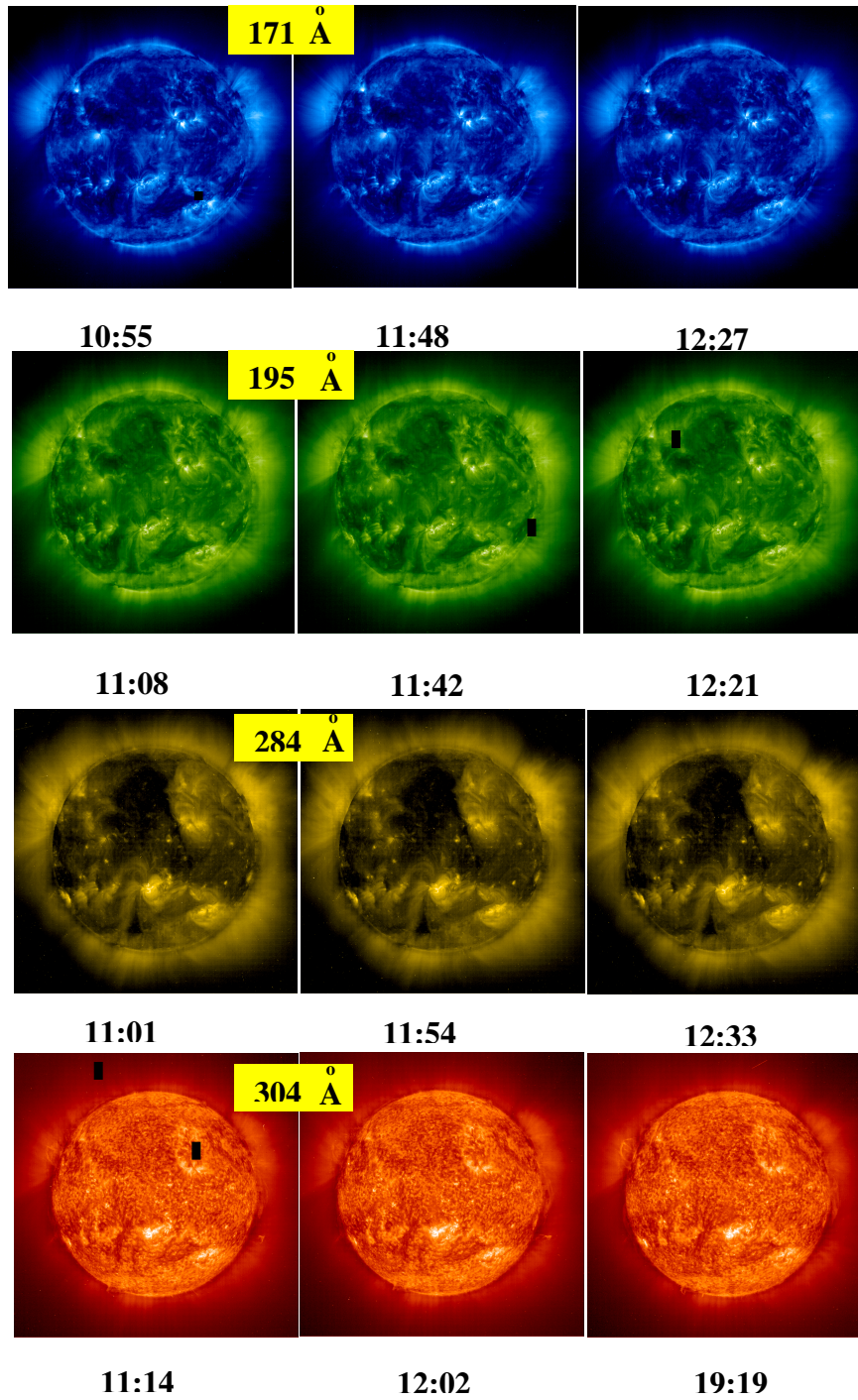


Figure (4.14). Images of the sun taken by the EIT instrument on SOHO on the 11 August 1999. The numbers denote the time in UT.

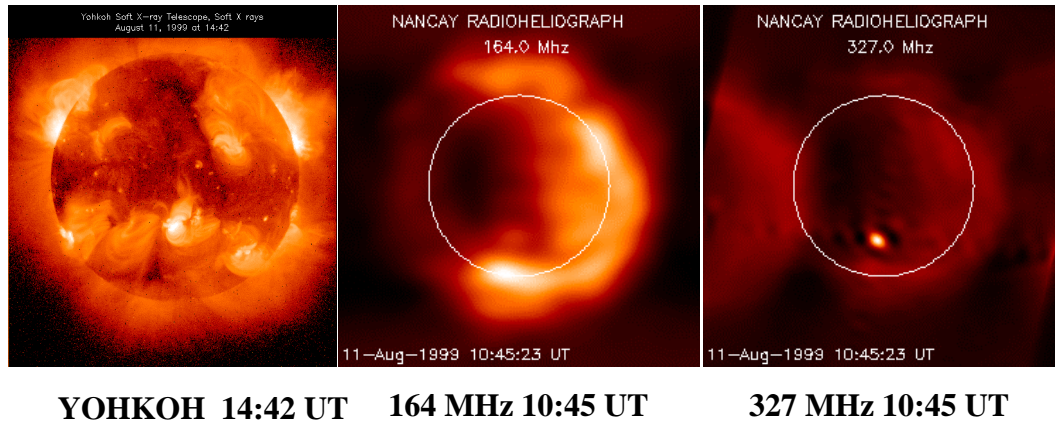


Figure (4.15). Images of the sun taken by the radiograph in Nancy, France and the x-ray telescope on Yohkoh on the 11 August 1999.

In figure (4.13) the coronal images of the sun were obtained from the C2 and C3 coronagraphs, of the LASCO (Large Angle and Spectrometric Coronagraph) instrument on SOHO, providing coronal images of the sun from 2.0 – 6.0 solar radii and 3.7 – 32.0 solar radii, respectively. These pictures reveal large-scale activities in the form of streamers in the southeast limb as compared to the rest of the limb. From figure (4.12) the fibers #19, 20, 21 and 22 were located in this region of high streamer activity.

In figure (4.14) are EIT (Extreme ultraviolet Imaging Telescope) on SOHO are images of the sun through various filters centered at different wavelengths as indicated on the images. These are images, through selected bandpasses in Fe IX/X at 171.0 \AA , Fe XII at 195.0 \AA , Fe XV at 284.0 \AA and He II at 304.0 \AA , reflect temperatures of $\sim 1.0 \text{ MK}$, $\sim 2.0 \text{ MK}$, $\sim 3.0 \text{ MK}$ and $\sim 4.0 \text{ MK}$, respectively.

In figure (4.15) are radio images from Nancy, France and a x-ray image from Yohkoh. The radio image in the center reveals that the east limb was either hotter or lesser in electron number density than the west limb. The bright spot on the image on the right shows the subflare #8662 reported at south14 east04 on 11 August 1999.

4.4 The telescope-spectrometer sensitivity curve

In section 4.4 the wavelength correction factor to convert terrestrial intensity observation to extraterrestrial intensity is discussed. The intensity recorded by MACS differs from the extraterrestrial intensity primarily due to the following two reasons.

1. The wavelength dependency of the physical parameters such as transmission efficiency, focal length, dispersion and quantum efficiency, etc of the optical components of MACS.
2. The wavelength dependency of the measured coronal intensity on the transmission efficiency and the scattering in the earth's atmosphere.

In order to find a correction term to convert terrestrial intensity observation to extraterrestrial intensity for each of the fibers the following steps were followed. This follows the procedure adopted by Ichimoto et al. (1996).

1. The dark-current subtracted terrestrial sky spectrum observed by each fiber was corrected for Rayleigh scattering (λ^{-4}). The sky represents the F-component of the solar spectrum and also closely resembles the solar spectrum itself. However the Rayleigh scattering affects the overall distribution of the sky spectrum. Thus the Rayleigh corrected sky spectrum was assumed to closely represent the terrestrial solar spectrum at the observation site. Figure (4.16) shows the sky spectrum recorded by fiber #06 before and after correcting for Rayleigh scattering.

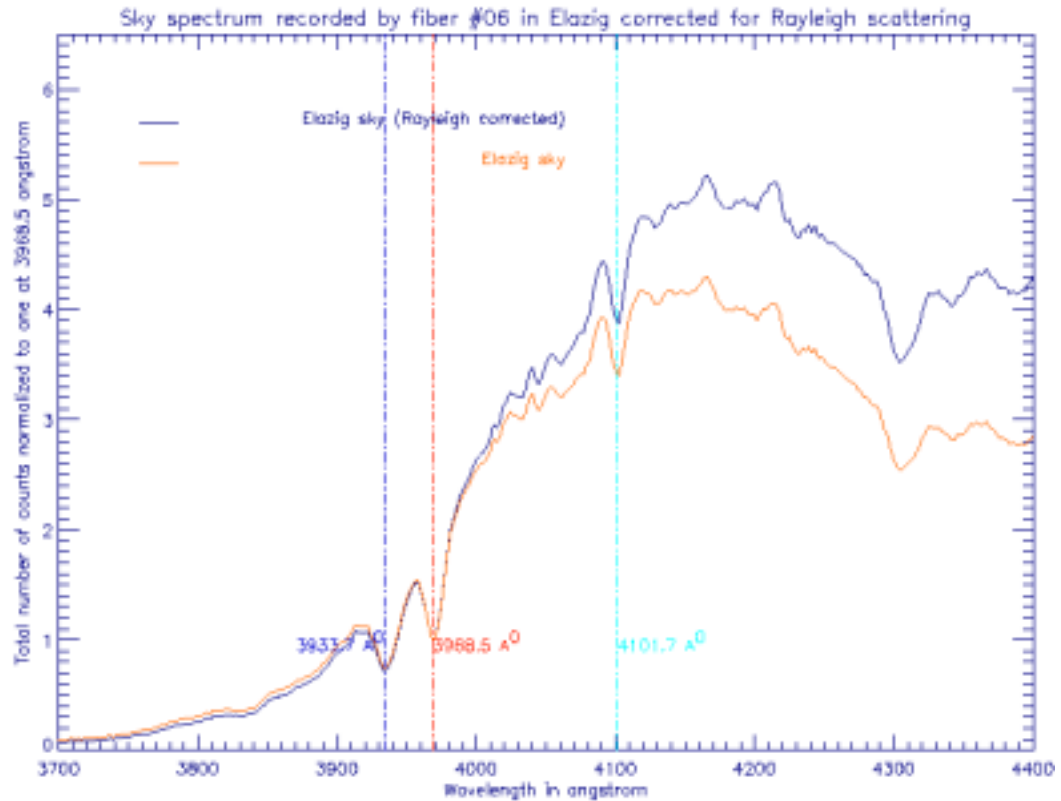


Figure (4.16). Plots of the sky spectrum recorded by fiber #06 in Elazig, Turkey before and after correcting for Rayleigh scattering. The plots have been normalized at 3968.5 Angstrom.

2. The terrestrial photospheric spectrum (Rayleigh corrected sky spectrum) recorded by MACS was calibrated with a wavelength scale using prominent absorption lines Ca II K & H at 3933.7 & 3968.5 angstrom, respectively and H_{δ} at 4101.7 angstrom. The positions of these absorption lines were matched with the corresponding positions of the same absorption lines in the extraterrestrial photospheric spectrum. These intensities were then divided by their respective intensities at 3968.5 angstrom. Figure (4.17) shows the terrestrial photospheric spectrum (Rayleigh corrected sky spectrum) recorded by fiber #06 and the extraterrestrial photospheric spectrum.

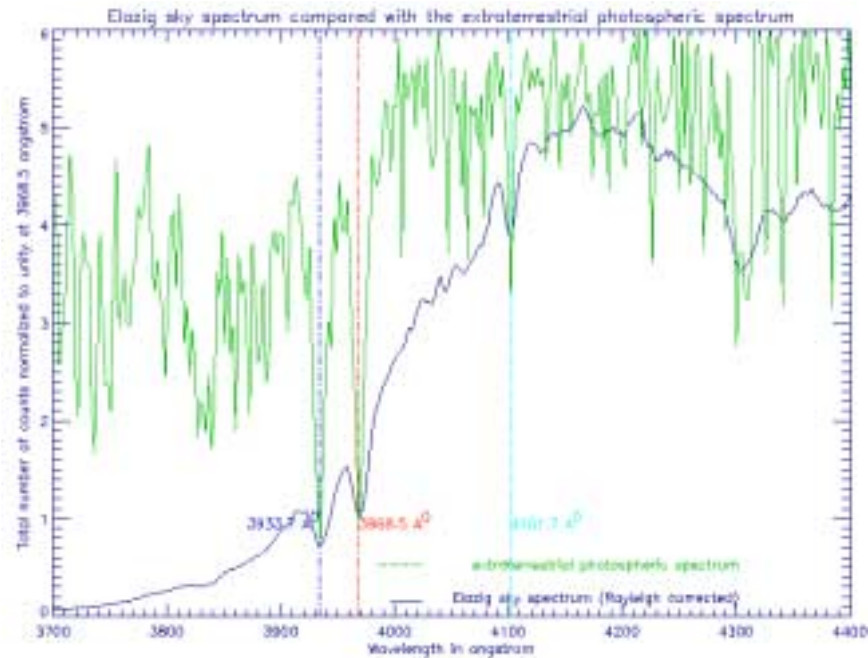


Figure (4.17). Plots of the extraterrestrial photospheric intensity spectrum and the terrestrial photospheric intensity spectrum recorded by fiber #06. The extraterrestrial photospheric spectrum is a smoothed version of the extraterrestrial photospheric spectrum shown in figure (2.1).

3. The extraterrestrial photospheric spectrum was smoothed until it matched the resolution of the terrestrial photospheric spectrum recorded by MACS. Figure (4.18) shows the terrestrial photospheric spectrum recorded by fiber #06 and the extraterrestrial photospheric spectrum smoothed in resolution to match the resolution of the terrestrial photospheric spectrum.

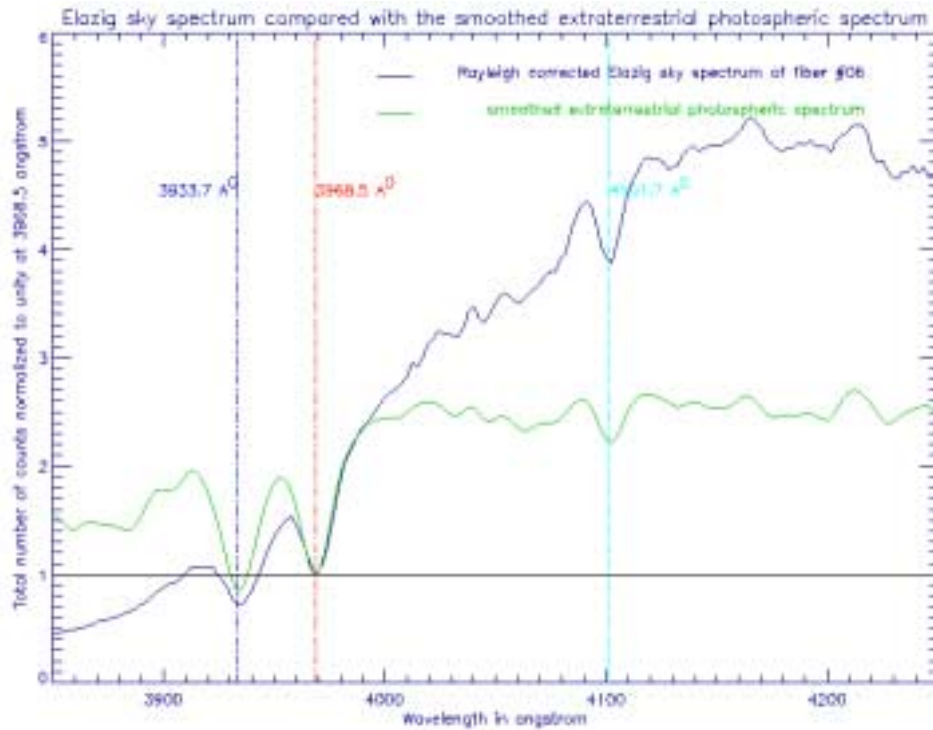


Figure (4.18). Plots of the smoothed extraterrestrial photospheric intensity spectrum and the terrestrial photospheric intensity spectrum recorded by fiber #06.

4. The ratios between the extraterrestrial and the terrestrial photospheric spectra were calculated against wavelength. Figure (4.19) shows plots of the smoothed extraterrestrial photospheric intensity spectrum, terrestrial photospheric intensity spectrum recorded by fiber #06 and the ratio between them.

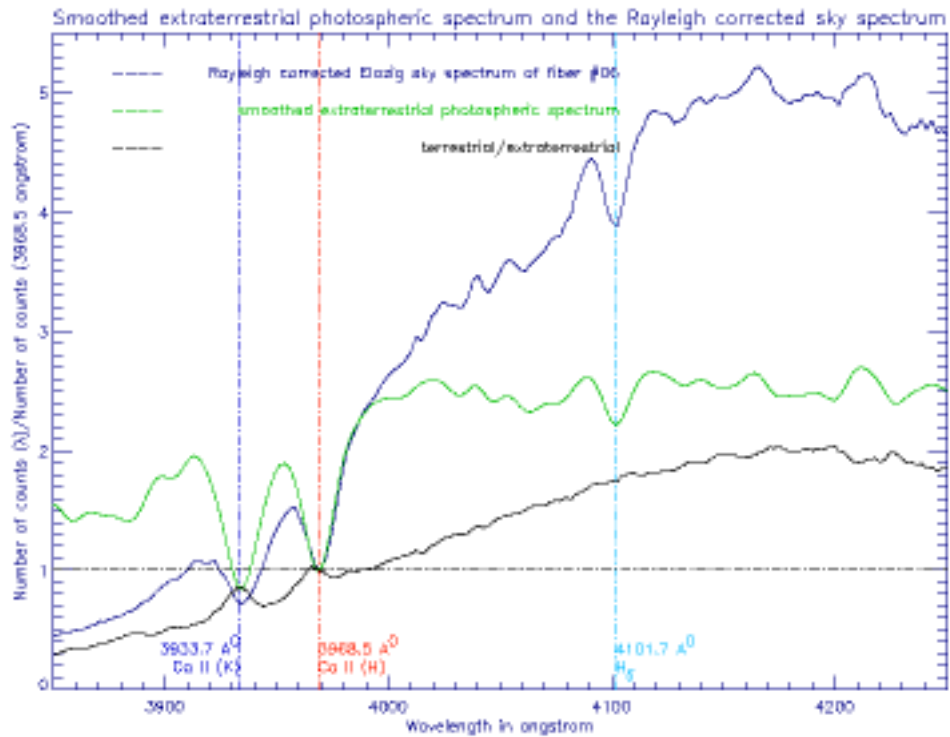


Figure (4.19). Plots of the smoothed extraterrestrial photospheric intensity spectrum, terrestrial photospheric intensity spectrum recorded by fiber #06 and the ratio between these two against wavelength.

5. A polynomial fit was made to the ratios between the extraterrestrial and the terrestrial photospheric spectra that were calculated against wavelength. Figure (4.20) shows the polynomial fit made to the ratio between the smoothed extraterrestrial photospheric intensity spectrum, and the terrestrial photospheric intensity spectrum recorded by fiber #06.

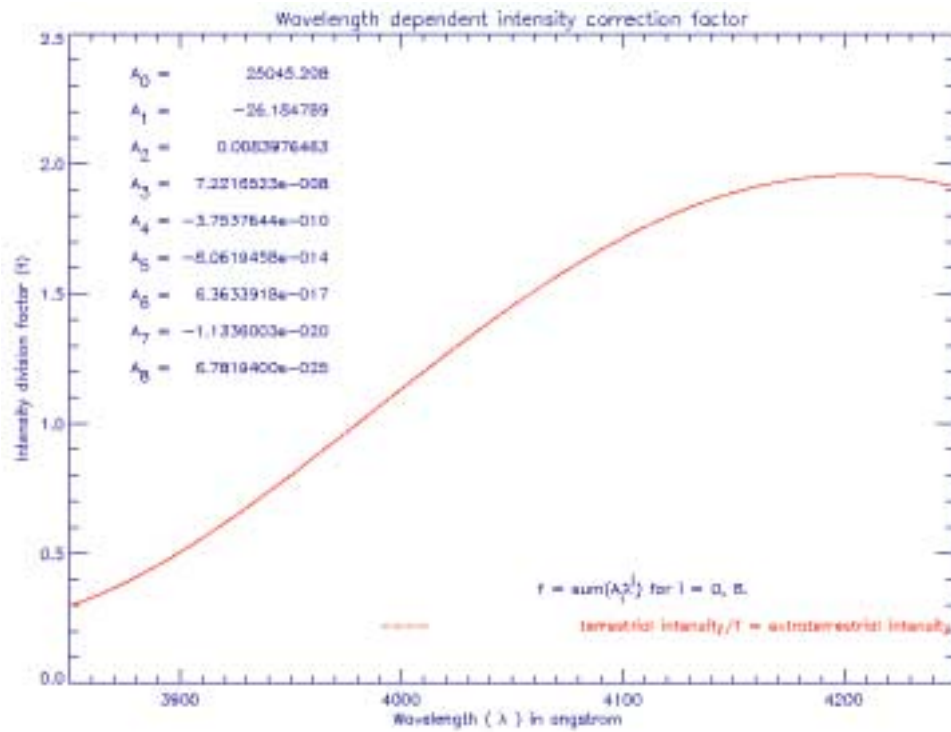


Figure (4.20). Polynomial fit made to the ratio between the extraterrestrial photospheric spectrum and the terrestrial photospheric intensity spectrum. The numbers on the plot are the coefficients of the polynomial fit.

Figure (4.21) shows the application of the polynomial fit to the terrestrial photospheric intensity spectrum to obtain the extraterrestrial photospheric intensity. This indicates a reasonably good fit. Also plotted in figure (4.12), for comparison purpose, is the smoothed extraterrestrial photospheric intensity spectrum as shown in figure (4.18).

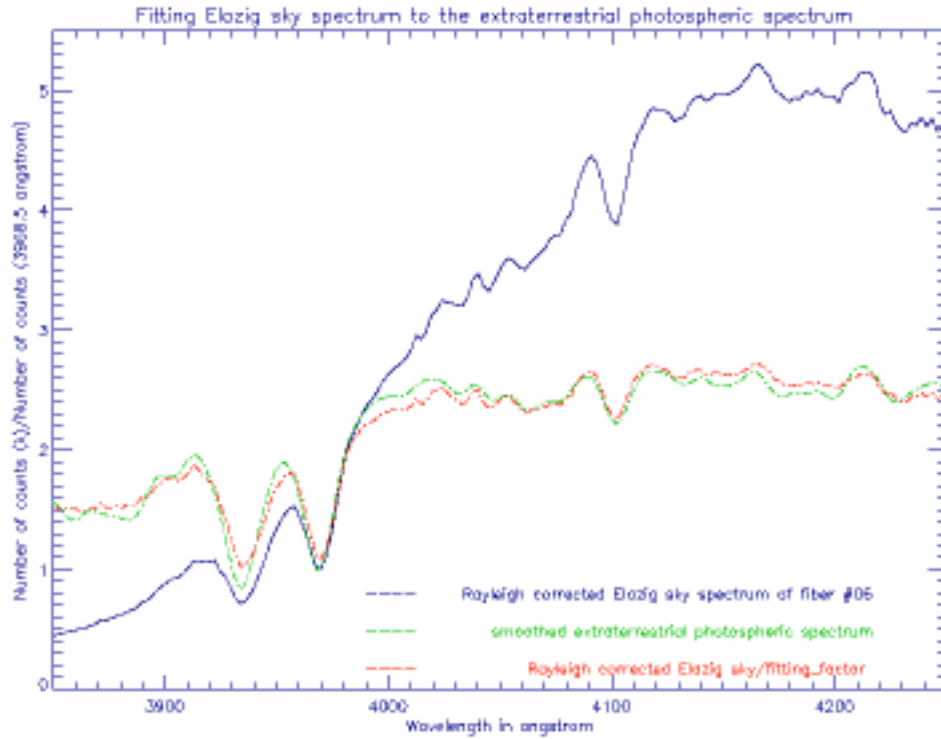


Figure (4.21). Application of the polynomial fit shown in figure (4.20) to the terrestrial photospheric intensity spectrum to obtain the extraterrestrial photospheric intensity. Also plotted for comparison purpose is the smoothed extraterrestrial photospheric intensity spectrum as shown in figure (4.18).

4.5 Application of the intensity correction factor

The extraterrestrial photospheric intensity spectrum differs from the terrestrial photospheric intensity spectrum measured by MACS primarily due to the atmosphere and the optical elements in MACS. Therefore the ratio between the extraterrestrial and the terrestrial photospheric intensity at a given wavelength could be written as shown in equation (4.1).

$$\frac{I_{PT}(\lambda)/I_{PT}(\lambda_0)}{I_{EX}(\lambda)/I_{EX}(\lambda_0)} = f(A, \tau) \equiv f(\lambda)$$

$\tau(\lambda)$ = transmission efficiency of MACS
 $A(\lambda)$ = atmospheric attenuation

(4.1)

where I_{PT} and I_{EX} are the photospheric intensity measured by MACS from ground and the extraterrestrial photospheric intensity, respectively. Here both the extraterrestrial and the terrestrial intensities are divided by their respective intensities at a reference wavelength λ_0 . In producing figure (4.18) the reference wavelength λ_0 was selected to be the Ca-II H line at 3968.5 angstrom. The same is true for the measurement of any other extraterrestrial intensity spectrum including the measurement of the solar coronal intensity measurement during an eclipse.

Using equation (4.1) the terrestrial coronal intensity at a given wavelength λ measured by MACS during the eclipse would correspond to the extraterrestrial coronal intensity given by equation (4.2).

$$\boxed{\begin{aligned} I_{EX}^C(\lambda) &= \frac{1}{f(\lambda)} \times \frac{I_{EX}^C(\lambda_0)}{I_G^C(\lambda_0)} \times I_G^C(\lambda) \\ I_G^C(\lambda) &= \text{terrestrial coronal intensity} \\ I_{EX}^C(\lambda) &= \text{extraterrestrial coronal intensity} \end{aligned}} \quad (4.2)$$

From equation (4.2) the extraterrestrial coronal intensity ratio at wavelengths λ_1 and λ_2 is given by equation (4.3).

$$\boxed{\frac{I_{EX}^C(\lambda_1)}{I_{EX}^C(\lambda_2)} = \frac{f(\lambda_2)}{f(\lambda_1)} \times \frac{I_G^C(\lambda_1)}{I_G^C(\lambda_2)}} \quad (4.3)$$

4.6 Determination of the Thermal electron temperature and the Solar wind velocity for each fiber location

The coronal spectrum recorded by each fiber contains the K, F and E coronal spectra. In order to determine the thermal electron temperature and the solar wind velocity, as per the methodology discussed in chapter-2, the K-coronal spectrum has to be isolated. Figure (4.22) shows the coronal spectrum recorded by the twenty-one fibers in the 18.0 seconds exposure.

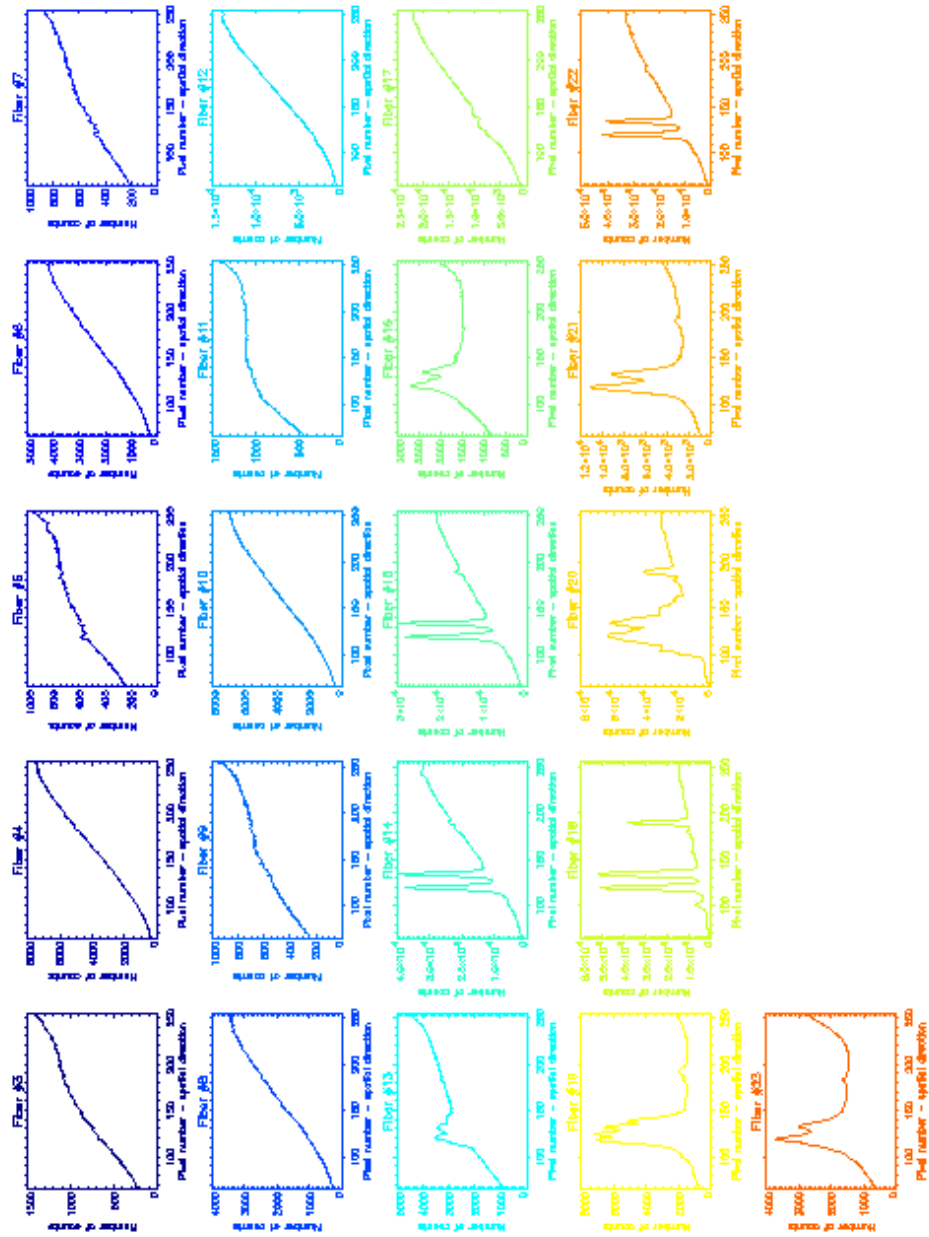


Figure (4.22). These plots show the coronal spectra recorded by the twenty-one fibers located at various latitudes and heights on the corona as depicted in figure (4.12). Fiber #23 was centered on the moon. The above spectra were recorded in the 18.0 seconds exposure. The x-coordinate is in pixel units.

Comparison between figure (4.22) and (4.12) it is evident that the fibers below the equator prominently display emission lines. From fiber #23, which was located at the center of the moon, was expected to record the background counts in addition to the coronal light reflected off the clouds and re-reflected off the moon. However the observational site in Elazig, Turkey reportedly being free of clouds the spectrum from fiber #23 only reveals the extent of the instrumental stray light. This stray light is believed, largely, to have originated in the telescope and could pose a significant error in the wind measurement. This is because the scattering is significantly large in the bright end of the spectrum in MACS. This in turn could give a larger count number for the intensity at 4233.0 angstrom, which is used in determining the wind sensitive intensity ratio. This is evident in the spectrum of fiber #23. In this regard it is prudent to eliminate at least 1-% of the counts in the bright end of the spectrum. The fibers recording emission lines can be attributed to exposure to prominence spectrum as discussed in section (4.3).

Figure (4.23) is the coronal spectrum recorded by fiber #06. As per figure (4.12) this fiber was located midway between the solar equator and the solar North Pole at 1.1 solar radii. Also LASCO images in figure (4.13) confirm this region free of streamer activities. The following steps were carried out in order to isolate the K-coronal spectrum in fiber #06 and closely resemble the methodology described by Ichimoto et.al (1996).

1. It was assumed that the Rayleigh corrected sky spectrum to closely resemble the F-component of the solar spectrum. On this basis a fraction of the sky component corresponding to about 1-% of the counts at 4250.0 angstrom in the coronal spectrum was subtracted.

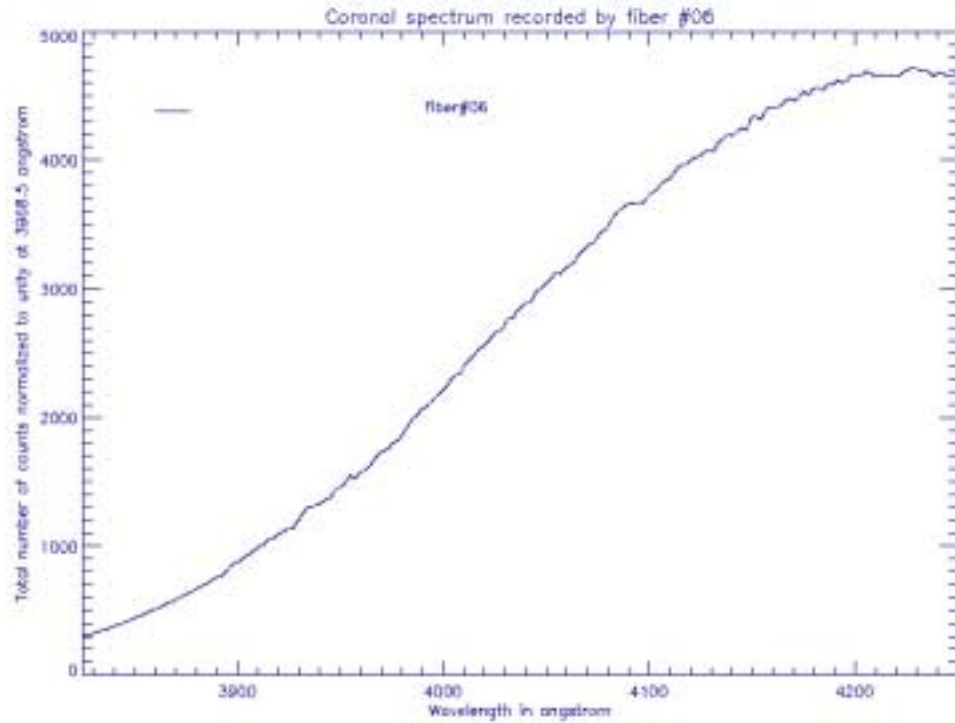


Figure (4.23). The coronal spectrum recorded by fiber #06.

2. A third order polynomial fit was made to the difference between the coronal spectrum subtracted by the F-coronal spectrum. This was possible in the above case since the coronal spectrum of fiber #06 is devoid of any significant emission lines. In the cases with strong emission lines gaussian fits would be made and subtracted with the background added to the continuum. In order to account for the stray light a constant value was subtracted from the coronal spectrum in order to make the overall variation

with wavelength (the ratio of the average intensity in 3700-3800 angstrom and the intensity around 4250 angstrom) to be identical with that of the brightest spectrum recorded by a fiber. For fiber #06 this correction amounted to 55 digital units in a 16-bit dynamic range. Figure (4.24) shows the reduced K-coronal spectrum from fiber #06.

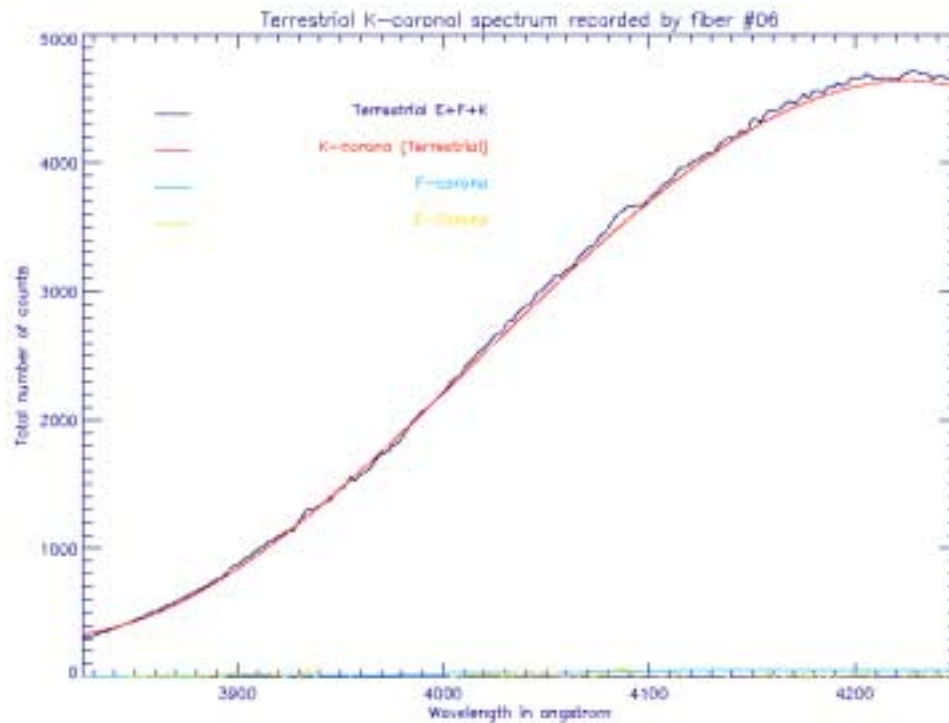


Figure (4.24). The terrestrial K-coronal spectrum reduced from the coronal spectrum recorded by fiber #06.

3. The terrestrial K-coronal spectrum was adjusted by the wavelength sensitivity curve in figure (4.20). This would transform the terrestrial K-coronal spectrum to the extraterrestrial K-coronal spectrum. This curve was used to determine the wind and the temperature sensitive ratios using equation (4.2). Figure (4.25)

shows the extraterrestrial K-coronal intensity derived for fiber #06 together with the wind and the temperature sensitive intensity ratios.

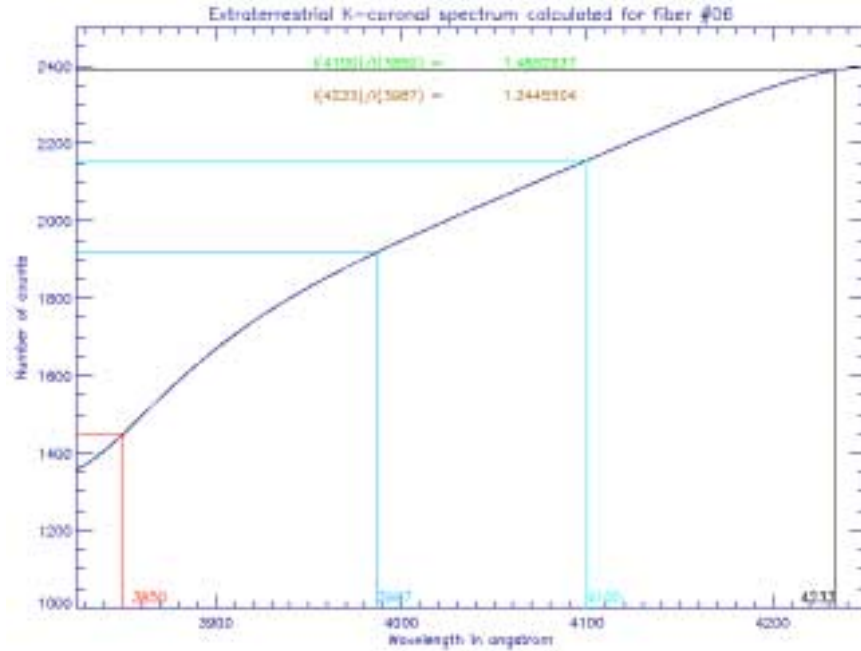


Figure (4.25). This plot shows the extraterrestrial K-coronal spectrum derived for fiber #06. The wind and the temperature sensitive intensity ratios are 1.245 and 1.488, respectively.

4. The theoretical temperature and the wind sensitive plots for the desired line of sight were then used to predict the thermal electron temperature and the solar wind velocity. The figure (4.26) and figure (4.27) show the locations of the temperature and the wind sensitive intensity ratios, derived from figure (4.25), on the theoretical thermal electron temperature and the solar wind velocity plots at 1.1 solar radii, respectively. These plots associate a thermal electron temperature of ~1.73 MK and a solar wind velocity of ~467.0 km/sec for fiber #06's location on the solar corona. The error bars will be discussed in section (4.7).

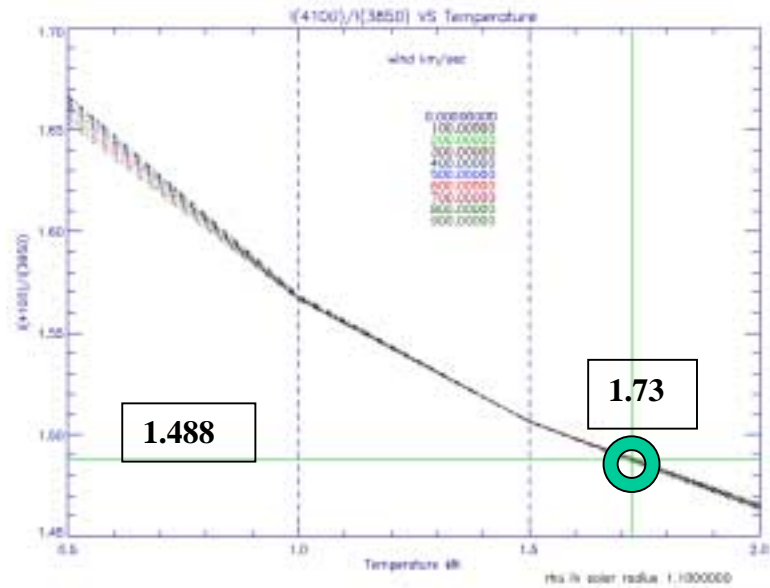


Figure (4.26). The temperature sensitive plot. This assigns a thermal electron temperature of ~1.73 MK for fiber #06.

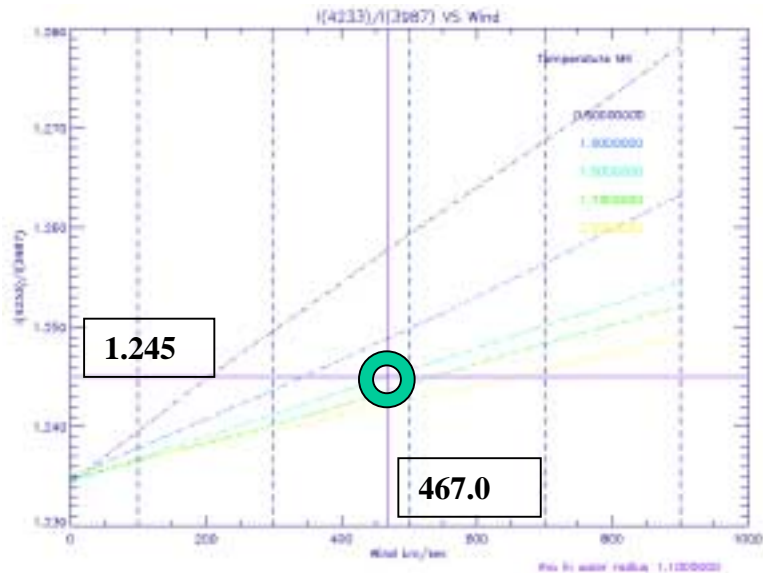


Figure (4.27). The wind sensitive plot. This assigns a solar wind velocity of ~467.0 km/sec for fiber #06.

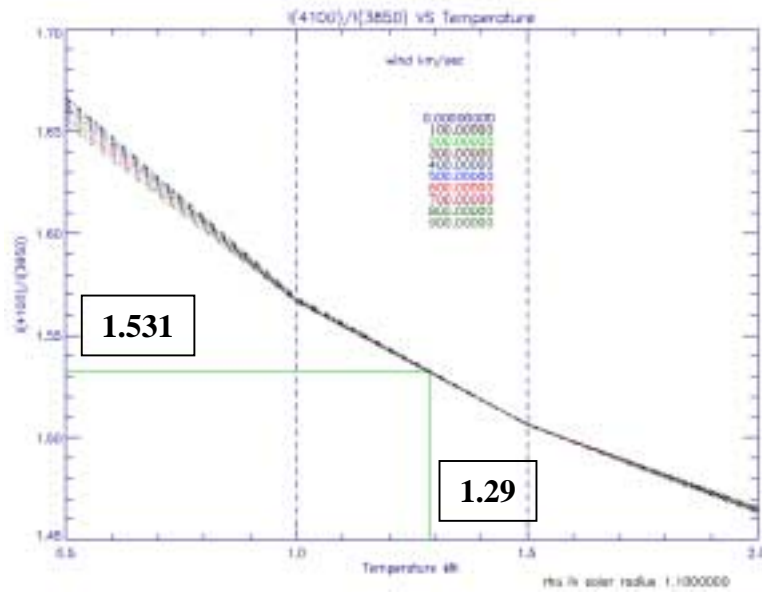


Figure (4.28). The temperature sensitive plot. This assigns a thermal electron temperature of ~1.29 MK for fiber #04.

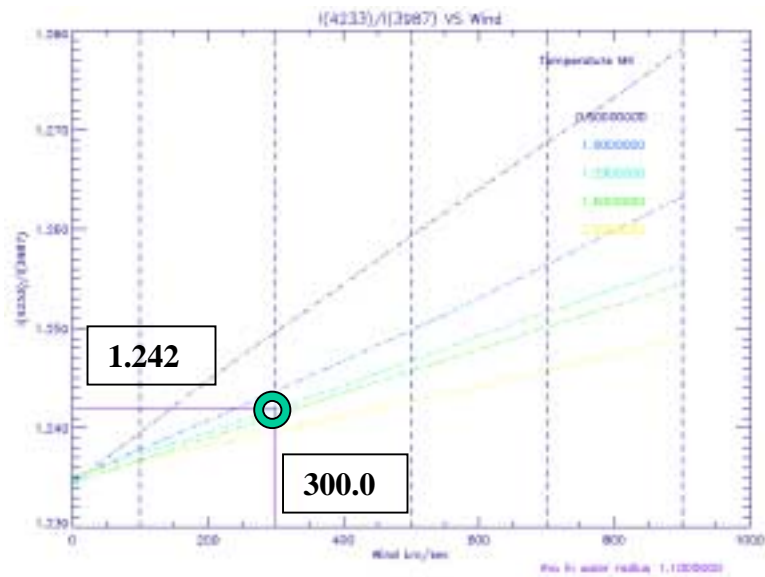


Figure (4.29). The wind sensitive plot. This assigns a solar wind velocity of ~300.0 km/sec for fiber #04.

Similarly figure (4.28) and figure (4.29) show the locations of the temperature and the wind sensitive intensity ratios on the theoretical thermal electron temperature and the solar wind velocity plots at 1.1 solar radii, respectively. These plots associate a thermal electron temperature of ~1.29 MK and a solar wind velocity of ~300.0 km/sec for fiber #06's location on the solar corona. Figure (4.30) shows the extraterrestrial K-coronal spectrum derived for fiber #10. Figure (4.31) and figure (4.32) give a thermal electron temperature of ~1.34 MK and a solar wind velocity of ~571.0 km/sec for fiber #10's location on the solar corona.

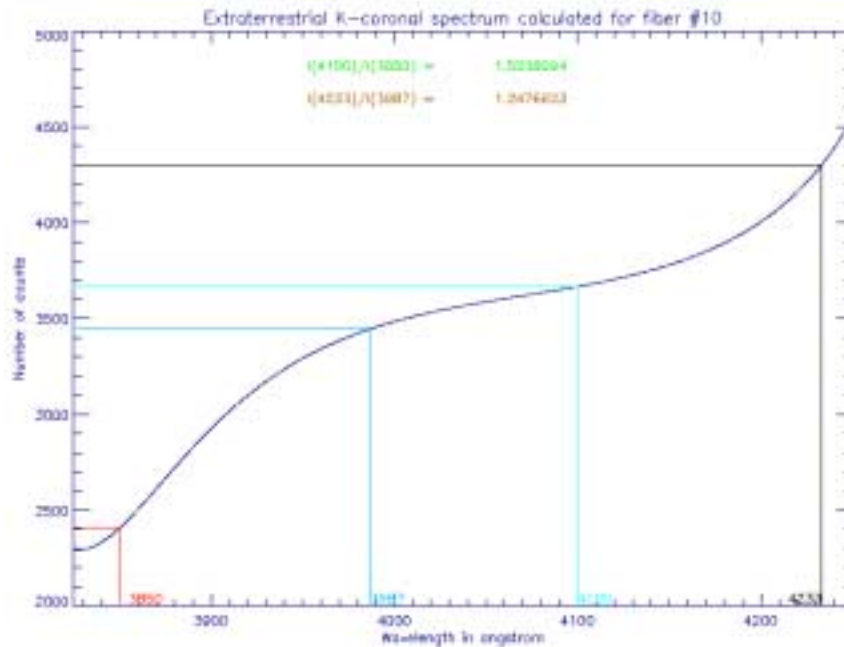


Figure (4.30). This plot shows the extraterrestrial K-coronal spectrum for fiber #10. The wind and the temperature sensitive intensity ratios are 1.248 and 1.524, respectively.

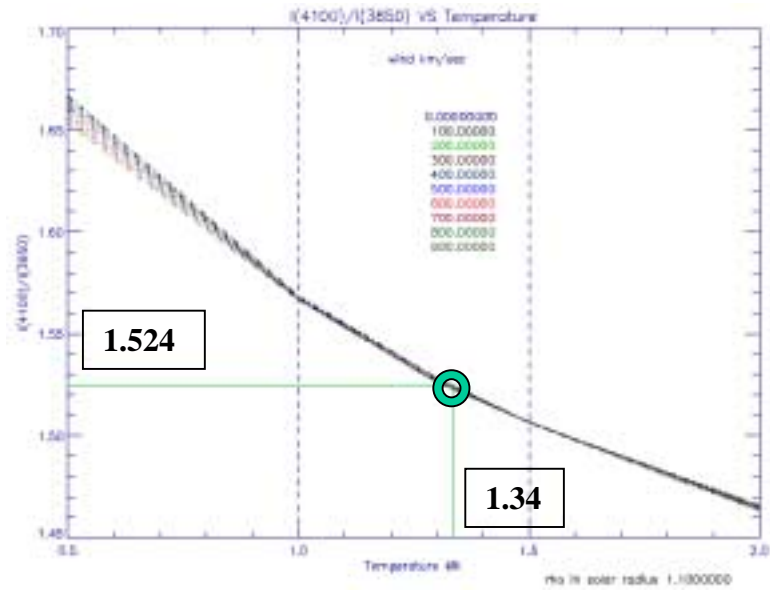


Figure (4.31). The temperature sensitive plot. This assigns a thermal electron temperature of ~1.34 MK for fiber #10.

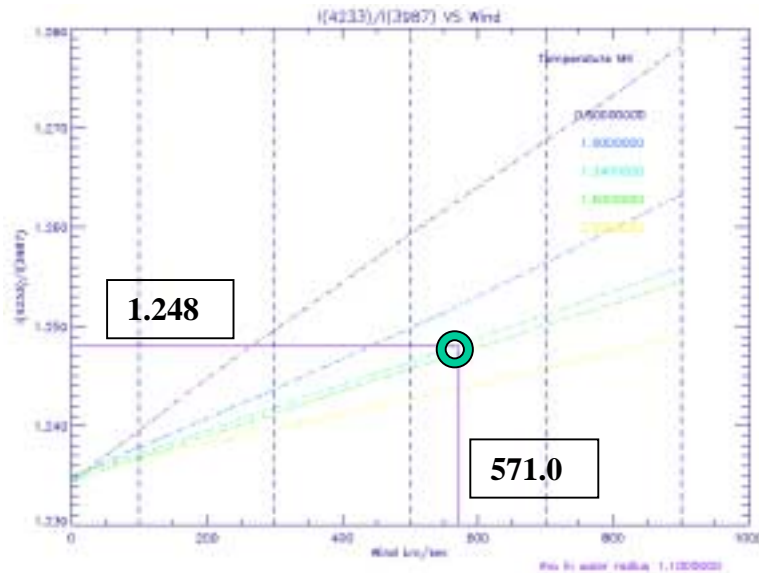


Figure (4.32). The wind sensitive plot. This assigns a solar wind velocity of ~571.0 km/sec for fiber #10.

Figure (4.33) shows the coronal spectrum recorded by fiber #14 that includes prominent emission lines in calcium and hydrogen. The continuum was obtained by fitting a gaussian function of the form given by equation (4.4) to the emission lines and fitting equation (4.5) to the continuum.

$$f(\lambda) = A_0 e^{-\frac{z^2}{2}} + A_3 + A_4 \lambda + A_5 \lambda^2 \quad \text{where} \quad Z = \left(\frac{x - A_1}{A_2} \right) \quad (4.4)$$

$$A_3 + A_4 \lambda + A_5 \lambda^2 \quad (4.5)$$

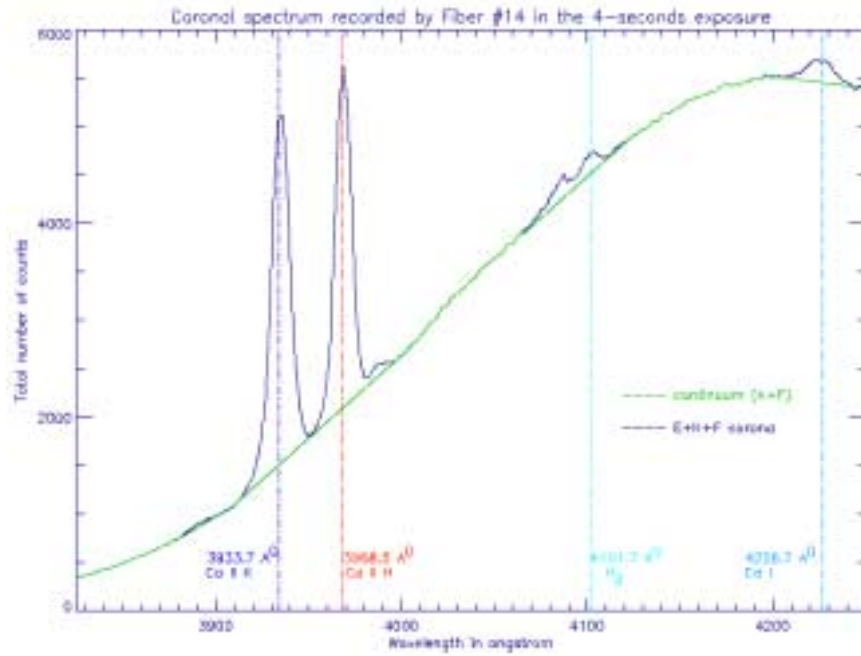


Figure (4.33). This plot shows the terrestrial coronal spectrum recorded by fiber #14. The continuum is a measure of the terrestrial F+K corona. The E-corona is removed by making Gaussian fits of the form given in equation (4.1) to the individual emission lines and fitting the background given by equation (4.2) to the continuum.

Following the steps described above figure (4.34) shows the extraterrestrial K-coronal spectrum reduced for fiber #14.

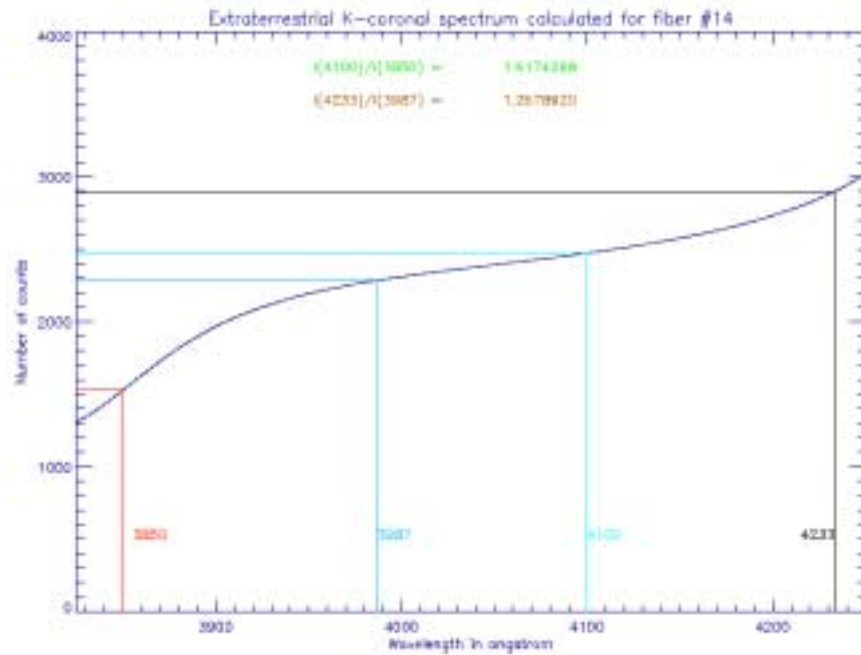


Figure (4.34). This plot shows the extraterrestrial K-coronal spectrum for fiber #14. This is following the elimination of the E-corona from figure (4.33).

From figure (4.35) and figure (4.36) the thermal electron temperature and the solar wind velocity derived for fiber #14 are ~ 0.73 MK and ~ 819.0 km/sec, respectively. However from figure (4.12) and figure (4.13) it is evident of a streamer and some bright structures in the field of view of fiber #14. This fairly low temperature could result from one of two possibilities. Firstly the fiber may have seen the corona very close to the limb based on the possibilities of errors arising from improper alignment of the fiber optic plate in the focal plane of the telescope or improper tracking.

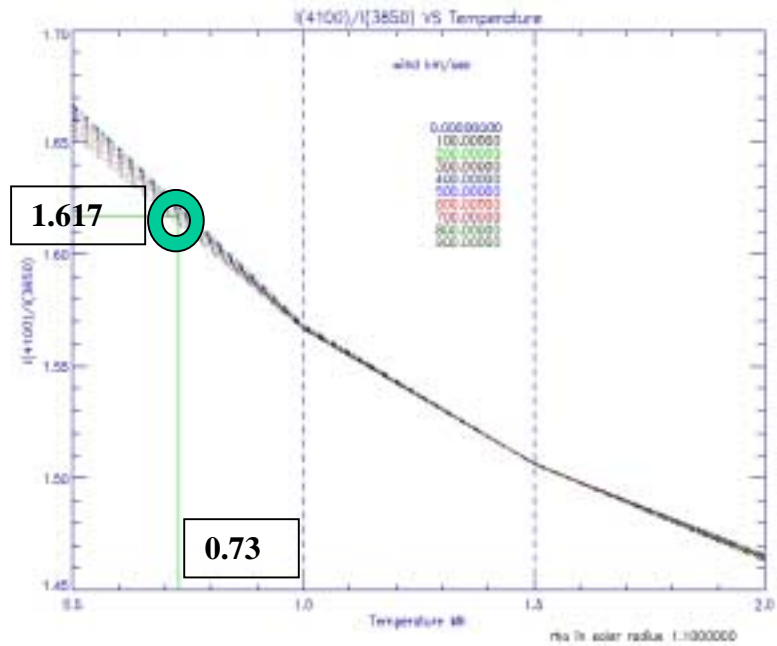


Figure (4.35) The temperature sensitive plot. This assigns a thermal electron temperature of ~0.73 MK for fiber #14.

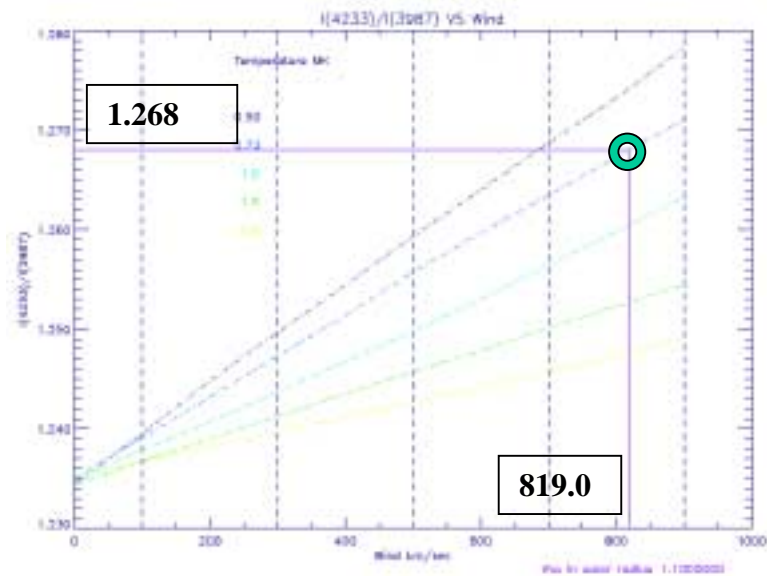


Figure (4.36). The wind sensitive plot. This assigns a solar wind velocity of ~819.0 km/sec for fiber #14.

Secondly, it is apparent that local density enhancement may have resulted at points of intersection of the streamer with the line of sight of fiber #14. Although the actual geometry nor the magnitude of the density enhancement are known, nevertheless, using a trial geometry and an assumed magnitude for density enhancement it can be shown that the temperature determined for fiber #14 may differ widely from the true value. This phenomenon is described in Appendix-C. In the following example the geometry described in Appendix-C was used along with an assumed density enhancement by a factor of 50.0.

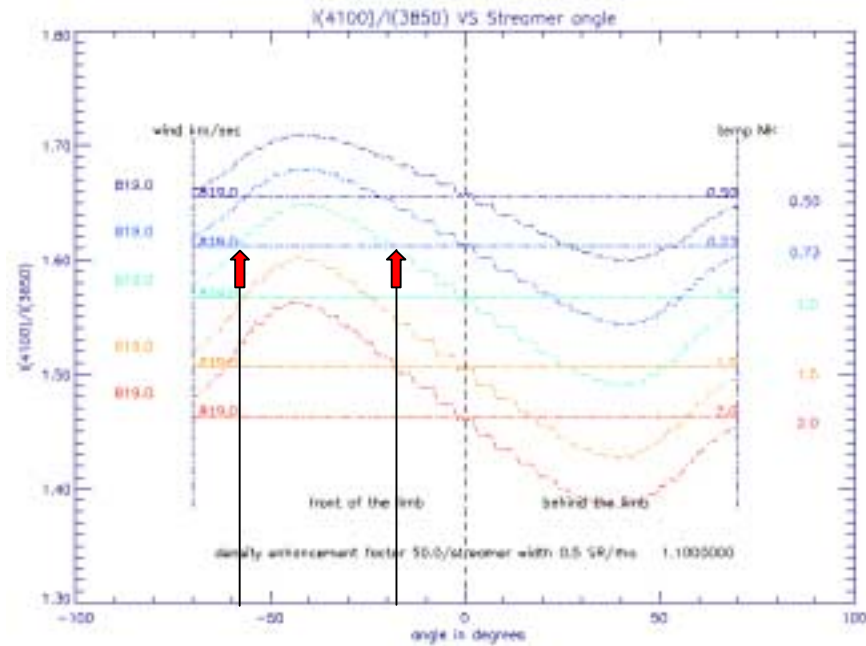


Figure (4.37). Plot showing the variation in the temperature-sensitive intensity ratio, from the theoretical models without streamers, for a streamer of geometry described in Appendix-C and density enhanced by a factor of 50.0 together with various streamer inclinations in front and behind the solar limb.

In figure (4.37) the horizontal lines show the temperature-sensitive intensity ratio for models without streamers. The curves with the matching colors show the variation of this ratio with streamers of the above geometry and density enhancement located at various angles in front and behind the limb. The two arrows indicate that a corona with temperature 1.0 MK and wind velocity 819.0 km/sec along with a streamer enhanced in density by a factor 50.0 and inclined at $\sim 18.0^\circ$ or $\sim 58.0^\circ$ degrees in front of the limb could have given the same temperature-sensitive intensity ratio as the theoretical model without streamers for an isothermal corona of temperature 0.73 MK and solar wind velocity 819.0 km/sec. This example shows the sensitivity of the streamers crossing the lines of sight of the fibers in determining the temperature and the wind velocity. However this cannot be considered a detrimental factor in the broader science of determining the density enhancement associated with streamers, their temperatures and velocities.

My belief for the low temperature recorded by fiber #14 has the following interpretation. From figure (4.1) and (4.14) it is apparent that the fiber #14 was closely placed to the extended prominence. It is very likely in this scenario that the line of sight integration for fiber #14 contained cool material associated with a prominence and is a signature of its likely temperature.

From similar analyses the schematic diagram in figure (4.38) shows the values determined for the thermal electron temperature and the solar wind velocity for fibers #04, 06, 08, 10, 12, 14 & 22 located at 1.1 solar radii and fiber #15 & 17 located at 1.5

solar radii. Unfortunately it has not been successful in determining the wind velocities for fibers # 15 and 22. The spectrum recorded by these fibers show a gradual decline in counts above 4200.0 angstrom for reasons, which are not obvious. All the temperature and wind values determined for the above fibers are based on the theoretical models without consideration for streamers.

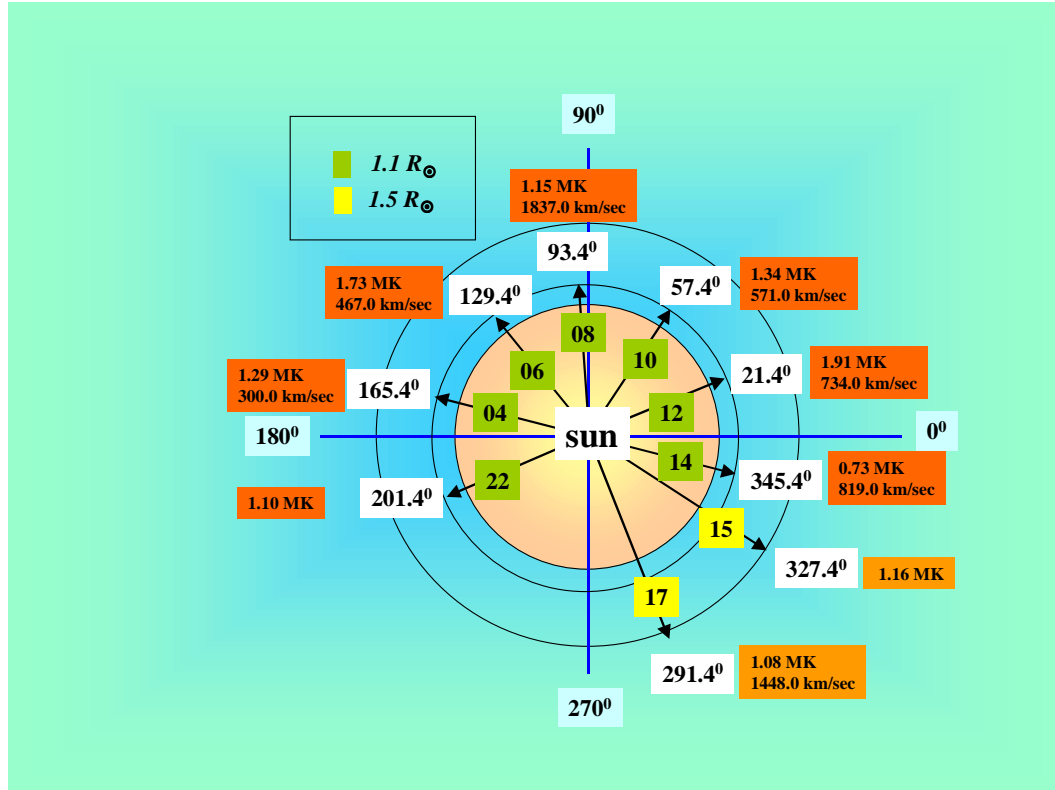


Figure (4.38). The thermal electron temperature and the solar wind velocity determined for solar coronal locations observed by fibers #04, 06, 08, 10, 12, 14 & 22 that are located at 1.1 solar radii and fiber #15 & 17 located at 1.5 solar radii. These values are based on the theoretical models. The temperature and the wind velocity are measured in MK and km/sec, respectively. However the wind measurements seem too far high. In this regard it is acknowledged that the experiment was not successful in measuring the wind velocities and the absolute values should be disregarded.

4.7 Sources of error and error bars

The sources of systematic errors could have resulted from improper alignment of the fiber optic plate in the focal plane of the telescope and tracking inadequacies. These practical reasons for these problems in the present status of MACS are highlighted in chapter-7 with suggested remedial measures.

Another disappointment in this experiment reflects from the spectrum recorded by fiber #23, which was centered in the center of the lunar shadow to record the background counts. The spectrum recorded by fiber #23, which was intended to measure the background counts, is shown in figure (4.39).

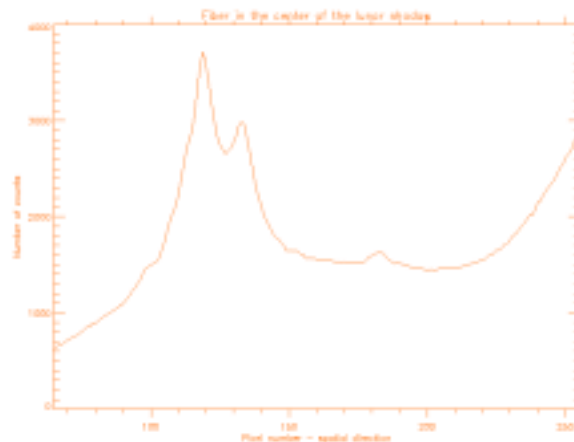


Figure (4.39). The spectrum recorded by fiber #23, which was centered on the lunar shadow during the eclipse. Its purpose was to measure the background counts.

Figure (4.39) highlights the scale of the instrumental scattering specially in the high end of the wavelength region that is sensitive to the wind-sensitive intensity ratio giving a higher count at 4233.0 angstrom. An attempt to quantify its influence on the spectra recorded by the other fibers is given in chapter-6. This may be the reason for obtaining very large measurements for the wind velocities. The wind velocities expected at 1.1 solar radii are of the order of ~ 100.0 km/sec. In this regard the absolute values determined for the wind velocities should be disregarded. However the ratios of the wind velocities in the equatorial regions to the coronal hole regions do make sense where the wind velocities at the poles are of the order ~ 3.0 times the wind velocities in the equatorial regions. Instrumental scattering could also be responsible for causing the coronal light recorded by a number of fibers unusable for analyses.

However scattering is an inevitable consequence arising from the financial constraints associated with obtaining superior optics. Also in respect to the time constraint associated with the eclipse duration it was not possible to do repeat measurements for random statistics. However this effort will be feasible with MACS attached to a coronagraph.

As for the temperature-sensitive intensity ratio one of the concern was the association of the wavelength positions to be in close proximity to strong emission lines. For example the proximity of the 4100 angstrom wavelength position to the emission line of H_{δ} at 4101.7 angstrom.

In addition there is also an error associated with the derivation of the instrumental wavelength sensitivity curve. Figure (4.21) shows the application of the wavelength sensitivity curve to the Rayleigh corrected sky spectrum to obtain the extraterrestrial photospheric spectrum (red curve). Matching this extraterrestrial photospheric spectrum (red curve) with what is considered as the true extraterrestrial photospheric spectrum (green curve), as depicted in figure (4.21), the overall deficiency is 0.44%. This is the difference between the area under these two curves. However this does not mean that point to point differences are as low as 0.44%. At the temperature-sensitive wavelength locations at 3850.0 and 4100.0 angstroms, these errors are -4.1% and $+1.9\%$, respectively. This can cause the temperature to be under estimated by 5.7% , which translates to 1.14 MK . The ideal remedy to this problem is an absolute wavelength calibration of MACS with sources of known strengths. However this does not still account for the instrumental scattering.

Although no clouds were reported during observation, yet the haze due to convection that is associated with the very dry terrain in Elazig, Turkey is another hidden consequence on the accurate coronal brightness measurements.

The influence of the numerical procedure and other physical parameters, such as the electron number density profile, used in creating the shape of the K-coronal intensity spectrum is discussed in chapter-5.

4.8 Summary

It has been demonstrated that the concept of MACS could be used as an instrument for global and simultaneous measurements of the thermal electron temperature and the solar wind velocity in the solar corona. The inaugural mission of MACS was beset with problems associated with instrumental scattering, lacking an imaging device to image the eclipse to ascertain tracking reliability and the possible atmospheric dust pollution due to the experimental location in a dry terrain devoid of vegetation. However the remedial measures are very simple in nature and tied to adequate financial resources. Using MACS with a coronagraph will also eliminate the time and terrain constraints associated with eclipses. Using MACS in a space platform that could take it very close to the solar surface and look into the corona will also eliminate the need for a coronagraph and the problems associated with the F-corona. This would be very promising in light of the scattering and the F-corona concerns associated with terrestrial observations. The remedial measures and the uses of other platforms for MACS are detailed in chapter-7.